ELSEVIER

Contents lists available at ScienceDirect

Journal of Materials Processing Tech.

journal homepage: www.elsevier.com/locate/jmatprotec





Modeling the strength of aluminum extrusion transverse welds using the film theory of solid-state welding

Gregory Oberhausen, Daniel R. Cooper

Mechanical Engineering Department, University of Michigan, George G. Brown Laboratory, 2350 Hayward Street, 48109-2125 Ann Arbor, MI, USA

ARTICLE INFO

Associate Editor: S-J. Na

Keywords: Material efficiency Industry Decarbonization Charge welds Two-piece billets

ABSTRACT

Reducing production scrap is vital for decarbonizing the aluminum industry. In extrusion, the greatest source of scrap stems from removing profile sections containing transverse (charge) welds that are deemed too weak for their intended purpose. However, until now, there has been no predictive transverse weld strength model. This article establishes a transverse weld strength model as a function of billet properties and extrusion parameters. It extends the film theory of solid-state welding by enhancing Cooper and Allwood's plane strain model to consider non-plane strain deformations at the billet-billet interface. These enhancements are informed by analyzing oxide fragmentation patterns through shear lag modeling and microscopy of profiles extruded from anodized billets. Model predictions are assessed through shear tests on welds from single and two-piece billets, extruded into rod, bar, and multi-hollow profiles. The experiments reveal that negative surface expansions at the weld nose cause interface buckling and weaker welds, but both surface expansions and weld strengths increase with distance from the nose. In non-axisymmetric profiles, deformation conditions and strengths vary across, as well as along, the weld. Two-piece billet welds are longer but reach bulk strength long before weld termination. The model predicts these trends and shows that die pressures are sufficient for micro-extrusion of any exposed substrate through interface oxide cracks. This underscores the significance of interface strains in exposing substrate and determining the weld strength. The model can help increase process yields by determining minimum lengths of weak profile to scrap and aiding process optimization for increased weld strength.

1. Introduction

Increasing manufacturing process yields is a key decarbonization strategy for the aluminum industry (IEA, 2019). Extrusion represents one of the most important aluminum supply chains to decarbonize, as around 20% of all aluminum is extruded (Cullen and Allwood, 2013) and there is an increasing demand for extrusions driven by automotive and energy applications; e.g., extrusions for use in body and chassis structures (Aluminum Extruders Council, 2022), electric vehicle battery trays (Afseth, 2021), and solar panel frames (Lennon et al., 2022). There is significant scope for improving extrusion process yields. Oberhausen et al. (2022) estimate that up to 40% of all aluminum cast into extrusion billets is scrapped before completion in a product. They find the greatest source of scrap is the (partial) removal of the transverse (charge) weld from extruded profiles. Reducing transverse weld scrap must therefore be targeted as part of the transition towards a low-carbon extrusion supply chain.

Transverse welds form between consecutively extruded billets in

direct extrusion. The initially planar billet-billet interface is elongated as it passes through the die, forming tongue-shaped welds in the profile (Fig. 1) with the number of welds equal to the number of die ports.

Concern about weld integrity generates process scrap in single-piece billet extrusion and limits scrap reuse via two-piece billet extrusion. In single-piece billet extrusion, the weld is often not removed from profiles destined for low-load applications; e.g., concrete screed handles (Mag Specialties, 2019). However, standard practice is to remove the profile section containing the weld when the profile is destined for more high-performance applications. For instance, U.S. automotive OEMs insist on the removal of transverse welds (Ford Motor Company, 2014). Elsewhere, the weld rear may be left in the profile if deemed to have sufficient strength. Transverse weld scrap can account for up to 20% of the initial billet mass (Oberhausen et al., 2022). Scrap from billet log cutting can be re-used via a two-piece billet extrusion process – when two short billets are loaded into the container. However, because this process creates an additional weld between the two short billets, it is typically constrained to low-load applications, limiting the opportunity

E-mail address: drcooper@umich.edu (D.R. Cooper).

^{*} Corresponding author.

for its use (da Silva, 2016).

1.1. Previous work on reducing transverse weld scrap

Transverse weld scrap could be reduced by either decreasing the weld length, increasing the weld strength, or through more accurate predictions of the weld strength so that only the weaker regions of the weld that compromise part performance need to be removed. Several researchers have conducted parametric studies on the effect of extrusion process parameters on the weld length, typically demonstrating weld length reductions of up to 15% are possible. Due to the expense of physical experiments, these studies typically rely on using finite element models that have been experimentally validated for one set of parameters to then explore the wider parameter space. For solid profiles, Hatzenbichler and Buchmayr (2010) study axisymmetric extrusion of AA6082 using the DEFORM FEM software package. They find that reducing the extrusion ratio has the largest effect on reducing the weld length. In contrast, changes to the bearing length, ram velocity, and ram-billet friction are found to have an insignificant effect. Mahmoodkhani et al. (2014) also use DEFORM to study axisymmetric extrusion of solid (AA3003) profiles, finding that die angle reductions significantly reduce the weld length. Oberhausen et al. (2021) use experiments extruding clay billets into solid profiles to find that weld lengths can be reduced by decreasing the friction between the billet and the die and container. They also find the weld length increases with the cross-sectional perimeter to cross-sectional area ratio of the extruded profile. For hollow profiles, Zhang et al. (2017) study extrusion of AA7N01 using HyperXtrude FEM software. Like the case of solid

extrusion, they find that decreasing the extrusion ratio has a significant impact on reducing the weld length. They also find that increasing the port bridge diameter, welding chamber radius, and baffle plate height are all beneficial. Reggiani et al. (2013) study weld lengths in the extrusion of hollow (AA6060) profiles and emphasize the importance of the feeding port dimensions. Other studies have shown specifically the importance of the number and geometry of the die bridges (Yu et al., 2016a) and of the welding chamber and porthole height (Crosio et al., 2018). Chen et al. (2015) find that using bridges sharpened in the direction of the billet (described as "pyramid dies" by Chen et al.) significantly reduces the weld length. Recently, Oberhausen and Cooper (2023a) proposed using profiled dummy blocks to reduce the weld length in both solid and hollow profile extrusion. Profiled dummy blocks generate shorter welds by compensating for the differential metal flow across the billet cross-section and require the billet butt to remain unsheared between ram strokes.

Transverse weld strength modeling is a complimentary endeavor to reducing the weld length. For a given profile, weld strength modeling and optimization will allow the length of profile removed due to weld integrity concerns to be reduced or eliminated where safe to do so. If the weld length can be reduced through process adaption, then the weld strength model still provides a basis for evaluating whether the rear of the weld can be preserved. Multiple publications study the strength and microstructure of transverse welds. For example, den Bakker et al. (2016) and Tang et al. (2022) extract tensile test coupons from extruded profiles to evaluate the effect of the transverse weld on the lateral strength of hollow AA6082 aluminum and ZK60 magnesium profiles respectively. Elsewhere, Nanninga et al. (2011) evaluate the effect of the

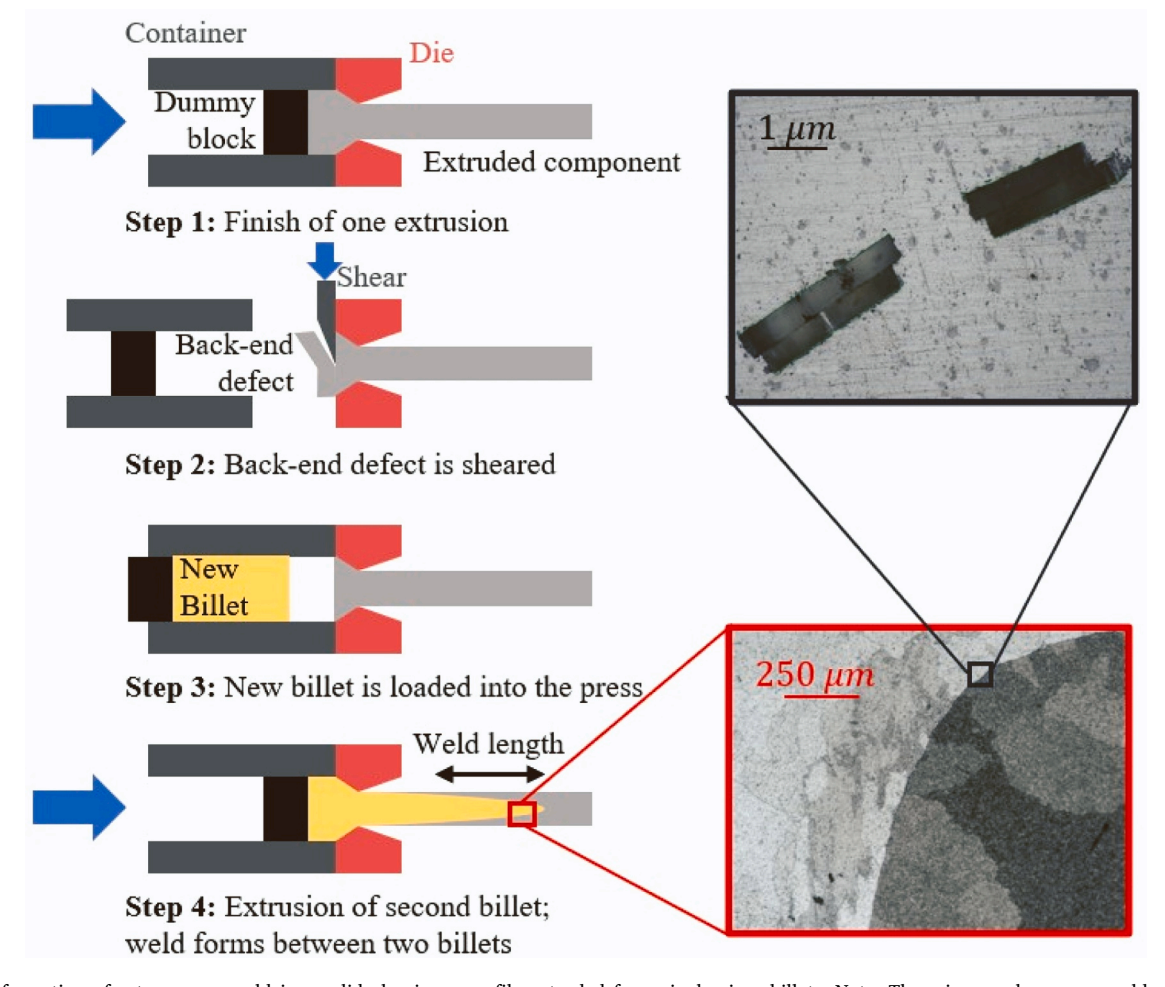


Fig. 1. The formation of a transverse weld in a solid aluminum profile extruded from single-piece billets. Note: The micrographs are on welds created using anodized billets.

transverse weld on the fatigue life of a AA6082 hollow profile. A consistent finding is that the ductility and strength increases towards the rear of the weld. This finding has been explained qualitatively by reference to either the changing microstructure (e.g., Yu et al., 2019) and/or oxide distribution (e.g., den Bakker et al., 2016). Lou et al. (2019) find that the outer billet material surrounding the nose of a AA6061 weld is composed of fine, equiaxed grains while the new billet material inside the nose is composed of long, thin grains. Further back in the weld, the grain structure of the new billet material more closely resembles that of the old billet. Similarly, Tang et al. (2022) and Yu et al. (2019) find that the nose of the weld is characterized by a coarse structure distinctly separated from old billet material by the bonding interface, but that the grains become increasingly uniform and span across the interface as the weld progresses and recrystallization increases.

The above articles have examined the transverse weld quality; however, to the authors' knowledge no transverse weld strength model exists that could be used to help determine whether a weld needs to be removed for a given application, to help estimate the minimum length of profile that must be scrapped to ensure the remaining profile contains only strong welds, and as part of a process optimization for increased weld strengths. Furthermore, in the literature the local weld strength has not been directly measured: previous work measures a proxy due to the difficulty of isolating the weld interface in the test coupon. Existing studies have focused on single-piece billet extrusion with use of a butt shear; however, transverse weld integrity concerns also limit two-piece billet extrusion applications. Additionally, some extruders still use presses without a butt shear (Mag Specialties, 2019) and for some new tooling concepts the billet butt is not sheared off (Oberhausen and Cooper, 2023a).

1.2. Candidate welding models for predicting the transverse weld strength

Over the last fifty years, several aluminum solid-state welding models have been proposed. For extrusion, researchers have focused on longitudinal welds in hollow profiles that form by the billet first splitting around the bridges in the porthole die and then rejoining before die exit (Xie et al., 1995). Longitudinal weld models predict if bonding has occurred based on whether a weld quality index exceeds some critical value. The index is calculated using deformation conditions at the interface. For example, Akeret (1972) proposed a maximum pressure criterion based on the peak normal contact stress at the interface. Plata and Piwnik (2000) introduced the pressure-time Q-criterion based on the integral of the ratio between the normal contact stress and effective stress over time. Later, Donati and Tomesani (2004, 2008) extended this further to the pressure-time-flow K-criterion to better account for the dead metal zones. They show the importance of high normal contact stresses to initiate bonding and to increase weld ductility. Yu et al. (2016b) introduced the J-criterion which also considers diffusion mechanisms for closing of micro-voids at the welding interface. Most recently, Kniazkin and Vlasov (2020) modified the Plata and Piwnik (2000) model to include the effect of the different material stream velocities flowing from different die ports.

Multiple studies have shown that the above welding models provide a good indication of longitudinal weld quality for both aluminum (e.g., Yu et al., 2016a) and magnesium alloys (e.g., Liu et al., 2017). However, these models are weld quality indicators rather than quantitative predictors of weld strength. Furthermore, with the exception of the transient state when extruding into an empty die (Wang et al., 2022), the rejoining metal streams in longitudinal welding are free of oxides (Zhang et al., 2013). In contrast, the billet-billet interface in transverse weld joining is covered in oxides. These oxides likely increase the importance of interface stretching for bonding to occur; oxide-to-oxide bonding does not occur below 1000 °C (Nicholas, 1990) and aluminum and its oxide are mutually insoluble, preventing cross interface diffusion of aluminum through the oxide films (Tylecote, 1968).

The importance of interface stretching is also indicated by those studies that use novel setups to mimic longitudinal welding by squeezing together two samples but that, due to the setup, have been unable to avoid sample oxidation before bonding. For example, Edwards et al., (2006, 2009) examine whether bonding has occurred after pushing together the ends of (radially unconstrained) aluminum rods and Bai et al., (2017, 2019) examine bonding of aluminum and magnesium bars pushed together in a tool that somewhat constrains spreading of the interface. These authors emphasize the importance of positive surface strains in achieving a bond in their experiments.

Examples of industrial solid-state welding processes where surface films are present include friction stir welding (FSW) and accumulative roll bonding (ARB). FSW is far from analogous to transverse weld formation as the stirring action in FSW causes a bulk material transfer across the interface (Cai et al., 2018). In ARB, sheets are stacked and then rolled, bonding them together as they pass through the roll bite (Saito et al., 1999). Bay (1983) proposed a weld strength model for cold roll bonding (plane strain deformation) based on the film theory of solid-state welding (Tylecote, 1968), which states that for welding to occur there must be intimate contact between clean metal surfaces. This necessitates that any surface films be broken to expose the reactive metal substrate (Ghalehbandi et al., 2019). With sufficient normal contact stress, the reactive substrate is then micro-extruded through cracks in the surface layer. If intimate contact between neighboring aluminum substrates of less than 10 atomic spacings is achieved then the attractive inter-atomic force will form a joint. Bay finds that a minimum expansion (threshold deformation) of the interface is required for any welding to occur in ARB. Cooper and Allwood (2014a) build upon Bay's film theory model, revising it for a range of temperatures and including the effect of local shear stresses on the true contact area between bonding surfaces as well as oxidation of substrate metal exposed early in the bonding process due to air entrapped between the surfaces. Cooper and Allwood evaluate their extension to Bay's model over a range of temperatures and normal contact stresses using near plane strain conditions, finding dispersed experimental weld strengths that trend as indicated by the model.

1.3. Scope of this work

While it is known that transverse weld strengths increase toward the rear of the weld, no predictive model of transverse weld strength exists. Longitudinal weld models are unsuitable because the oxides present during transverse weld formation are absent during longitudinal weld formation. In contrast, film theory models consider oxide fragmentation at the interface but have typically only been applied to (near) plane strain deformations, which are very different from the conditions at the billet-billet interface during extrusion. Therefore, the objectives of this paper are to extend the film theory of solid-state welding to predict the local transverse weld strength, to use the new model to identify the key determinants of the weld strength, and then to discuss the industry implications for reducing process scrap.

2. Derivation of the transverse weld strength model

This work builds on the mechanistic Cooper and Allwood (2014a) film theory model, defined in Eq. 1, and referred to from hereon as the C-A model. It assumes that the weld strength scales with the fraction of the interface area ($A_{nominal}$) that has bonded (A_{bonded}). The C-A model can be divided into three key terms, as shown in Fig. 2:

- The first term defines the fraction of the true versus nominal contact area, which is determined by the plastic flow at the asperity tip contacts induced by the normal contact stress (σ_n) and interface shear stress (τ_{app}) (Fig. 2a).
- ullet The second term (
 u) defines the fraction of the true contact area that consists of exposed substrate aluminum without a protective layer of

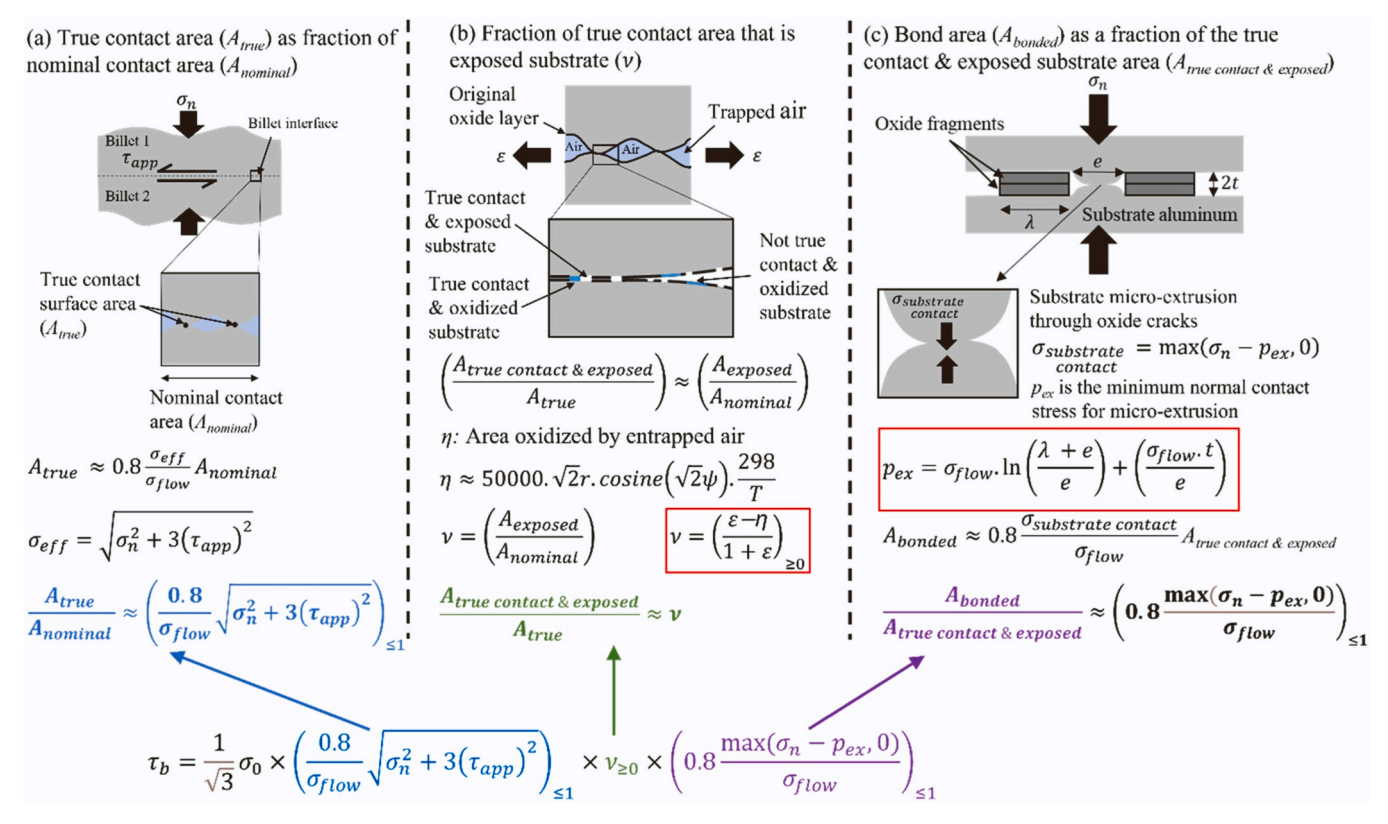


Fig. 2. The driving mechanisms of the original Cooper and Allwood (2014a) model. The equations for the model inputs highlighted in red must be updated to account for the non-plane strain deformation at the billet-billet interface during transverse weld formation. Figure inspired by Kolpak et al. (2019).

oxide. This term accounts for surface stretching and oxidation of initially exposed substrate by entrapped air (Fig. 2b).

• The third term defines the fraction of the exposed substrate on opposite sides of the interface that makes contact via micro-extrusion through the cracks in the oxide layer (Fig. 2c). This depends on the normal contact stress (σ_n), the flow stress of the substrate at the interface (σ_{flow}), and the minimum normal contact stress (p_{ex}) required to micro-extrude substrate aluminum through the oxide cracks. p_{ex} depends on the substrate flow stress and the oxide crack spacing (e) through which the substrate must micro-extrude.

The resulting weld shear strength (τ_b) is the product of the three terms discussed above and $\frac{1}{\sqrt{3}}\sigma_0$, where σ_0 is the bulk material room temperature tensile strength and the $\frac{1}{\sqrt{3}}$ coefficient converts from tensile to shear strength via the von Mises criterion.

$$\tau_b = \frac{1}{\sqrt{3}} \sigma_0 \left(\left(\frac{0.8}{\sigma_{flow}} \sqrt{\sigma_n^2 + 3(\tau_{app})^2} \right)_{\leq 1} . \nu_{\geq 0} . \left(0.8 \frac{\max(\sigma_n - p_{ex}, 0)}{\sigma_{flow}} \right)_{\leq 1} \right)$$

$$\tag{1}$$

Eq. 1 is applicable to a range of deformation conditions. However, calculations of key C-A model inputs (ν and p_{ex}) were originally defined by Cooper and Allwood assuming (near) plane strain deformation. This limits the welding interface to experiencing in-plane stretching in one direction and does not reflect the biaxial strain state at the billet-billet interface during extrusion. Updating this aspect of the C-A model is important as the strain state affects how the surface oxides fragment and therefore the exposed substrate area (ν) and the minimum normal contact stress for substrate micro-extrusion (p_{ex}).

In order to update the C-A model, four key assumptions are made about the biaxial oxide fragmentation at the billet-billet interface (A-D, below):

• When the local contact area expands, then:

- A. The length and width of the broken oxide fragments are equal and can be predicted using shear lag modeling.
- B. The broken oxide fragments are evenly spaced (locally) across the interface.
- C. The interface oxides break-up using a mix of coherent and incoherent fragmentation modes. Coherent fragmentation is when the oxides on opposite sides of the interface break-up at the same location, and incoherent fragmentation is when the oxides on opposite sides of the interface break-up at different locations.
- When the local contact area contracts, then:
 - D. The local interface buckles, oxide cracking is limited, and no welding occurs.

This article first shows that assumptions A-D are justified by studying the fragmentation of billet-billet interface oxides (Section 2.1). The validated assumptions are used to revise the calculations of key C-A model inputs (ν and p_{ex} , Section 2.2.), and the article then defines how the updated model is used to predict local transverse weld strengths (Section 2.3). This model is consistent with the film theory of solid-state welding. Diffusion also plays a key role in many solid-bonding processes (Cooper and Allwood, 2014b) (e.g., aluminum powder processing and superplastic diffusion bonding); however, it is unlikely to be a key mechanism in high strain rate conventional extrusion, where processing times are short as the interface passes through the die (Wu et al., 1998). The strength of the weld will be affected by the local microstructure. In this article, as implicitly assumed in other film theory based work such as Bay (1983) and Bambach et al. (2014), it is assumed that the film theory of solid-state welding, which is focused on the degree of bonding, is a good predictor of the weld strength when used to compare the weld strength against the strength of adjacent bulk material that has undergone similar deformation.

2.1. Testing the new model assumptions: Fragmentation of billet-billet interface oxides

As part of assumption A, shear lag modeling is used to predict the length of the broken oxide fragments on the transverse weld (Section 2.1.1). Assumptions A-D are then tested by examining the oxide fragmentation patterns produced on welds extruded using anodized billets (Section 2.1.2).

2.1.1. Shear lag model to predict oxide fragmentation

Building on the work of Agrawal and Raj (1989) and Le et al. (2004) on fracture of brittle films on ductile substrates, a simple shear lag model is used to estimate the oxide fragment size distribution for the case of local area expansion at the billet-billet interface. Fig. 3a shows the contact between consecutively extruded billets with a normal contact stress squeezing the surfaces together and tensile stretching in the axial direction creating an initial oxide fragment of length L. Surface stretching induces plastic deformation of the ductile aluminum substrate beneath the brittle oxide, which creates a shear stress at the substrate-oxide interface up to the ideal (substrate) shear strength of the interface ($k_{aluminum}$) and which reverses direction at the center of the oxide fragment. Force equilibrium dictates that a tensile stress (σ_t) is developed within the oxide layer that is inversely proportional to the oxide thickness (t_{oxide}) and increases with the distance from any existing cracks (Fig. 3b). The oxide can fragment wherever the tensile stress reaches the fracture strength of the oxide ($\sigma_{f,oxide} \approx 240MPa$), corresponding to region C-C' in Fig. 3b. As the interface is stretched, new cracks will continue to form, and the oxides get shorter until the oxide fragments are sufficiently small that the tensile stress in the oxide is always smaller than the oxide fracture strength. At this point the oxides have reached a stable size. The minimum oxide length occurs when a new crack forms at position C in Fig. 3b (a distance λ_1 from the adjacent crack) and the maximum oxide length occurs when a new crack forms at a distance $2\lambda_1$ from the adjacent crack. Subsequently, the minimum oxide fragment size is λ_1 and the maximum is $2\lambda_1$.

$$\lambda_1 = \sigma_{f,oxide} \cdot t_{oxide} / k_{aluminum} \tag{2}$$

$$\lambda_{average} = \frac{3.\sigma_{f,oxide} \cdot t_{oxide}}{2.k_{aluminum}} \tag{3}$$

As shown in Fig. 3c, the oxides may fragment coherently, where the oxides on opposite sides of the interface break-up together, or incoherently, where the oxides on opposite sides of the interface break-up at different locations. Coherent fragmentation should lead to greater weld strengths by increasing the area of the line-of-sight channels between the substrates on opposite sides of the interface, increasing the potential bonding area. It is hypothesized that a mix of coherent and incoherent oxide fragmentation modes occur in extrusion. Incoherent fragmentation is likely to be secondary because in that case oxide cracking on one side of the interface will be restrained by the frictional stresses acting from the neighboring uncracked oxide on the opposite side of the interface. This frictional restraint against cracking is not present if the oxides fragment coherently. Despite this, it is still expected that some incoherent fragmentation occurs due to oxides cracking before local interface contact and because any interface lubricity, which is difficult to eliminate in industrial settings, will reduce the frictional restraint against incoherent fragmentation.

2.1.2. Oxide fragmentation using anodized billets

Assumptions A-D are tested by observing oxide fragmentation at the billet-billet interface; however, native oxide fragmentation cannot be easily observed given that the native amorphous alumina layer is only around 2–10 nm thick (Evertsson et al., 2015) and that aluminum surfaces quickly reoxidize. Previously, Le et al. (2004) showed similar aspect ratios (oxide fragment length to thickness) are achieved in

fragmentation of anodized and native-grown oxide, concluding that anodized surfaces can be used to help study native oxide fragmentation. Therefore, single-piece and two-piece billets with anodized interfaces are extruded and the oxide fragmentation observed using optical microscopy on the final profiles. To anodize, the billets were faced-off on a lathe, polished, and chemically cleaned. The billets were then suspended in a sulfuric acid solution and charged with a current density of $160~\text{A/m}^2$ for 2 min to grow an oxide thickness of $0.9~\mu\text{m}$. Axisymmetric extrusion was performed using Ø3.5" (89 mm), 8" (203 mm) long anodized AA6061 billets at 425 °C at an extrusion ratio of 15. Two anodized 4" (101 mm) long billets were used in the same set-up for the two-piece billet test.

Fig. 4 shows the measured oxide size distributions at eight different locations examined across the two profiles. The oxide fragment aspect ratio is defined as the oxide fragment length divided by its thickness (0.9 μm in this case). In Figure 4, x^- and s represent the sample mean and standard deviation of the measured oxide fragment aspect ratios respectively.

Shear lag modeling (Eq. 2, with $k_{al}\approx 40 MPa$ and $t_{oxide}=0.9~\mu m$) predicts an oxide fragment aspect ratio of 5.4–10.8 and oxide fragment length of 4.8–9.7 μm . The experimental oxide size distributions in Fig. 4 are wider than the 1:2 minimum to maximum ratio implied by the shear lag modeling. This is likely due to varying experimental oxide thicknesses and fracture strengths. Even so, the mean oxide fragment aspect ratio (and length) is within the size distribution predicted by shear lag modeling for fifteen out of the sixteen location-orientation pairings shown in Fig. 4. The measured oxide size distributions in the axial and circumferential directions are also similar for all seven locations that correspond to local contact area expansion. Therefore, it is deemed reasonable that the length and width of the broken oxide fragments are modeled as equal and predictable using shear lag modeling, justifying assumption A.

Fig. 4 shows that the percentage of the weld line occupied by oxides is consistent in the axial and circumferential direction for all seven locations that correspond to local contact area expansion. Therefore, it is reasonable to assume that the broken oxide fragments are evenly spaced (locally) across the interface, justifying assumption B.

Fig. 5 shows representative microscopy images of the oxide fragmentation patterns. Optical microscopy of the weld lines shows that (near) complete coherent oxide fragmentation (Fig. 5a) was the primary fragmentation mode in the anodized billet trials, accounting for $\approx 75\%$ of all observed oxide fragmentation. Incoherent fragmentation (Fig. 5b) was found scattered across the welds, accounting for the remaining 25%. These observations justify assumption C that oxide break-up occurs with a mix of fragmentation modes.

The outlier in Fig. 4 is the circumferential distribution of oxides at the nose of the single-piece billet extrusion (12% new billet area). This corresponds to the only location in Fig. 4 to have experienced local contact area contraction during extrusion. Fig. 5c shows severe local buckling of the interface at this location, more oxide along the weld line than at any other tested location, and by far the highest mean oxide aspect ratio at 17. The weld in this location also possessed only handling strength, justifying assumption D. Further back in the single-piece billet weld, mean oxide fragment lengths are still longer in the circumferential than axial direction at 25% new billet area; however, by 41% new billet area there is not an appreciable difference between the oxide fragment size in the two directions. For the two-piece billet extrusion, all locations analyzed in Fig. 4 experienced local contact area expansion and there is negligible discrepancy at all points between the aspect ratio in the axial and circumferential directions.

2.2. Updating the C-A model

The anodized billet experiments validate the assumptions described in the Section 2 introduction. Using these assumptions, the calculation of the C-A model inputs is revised.

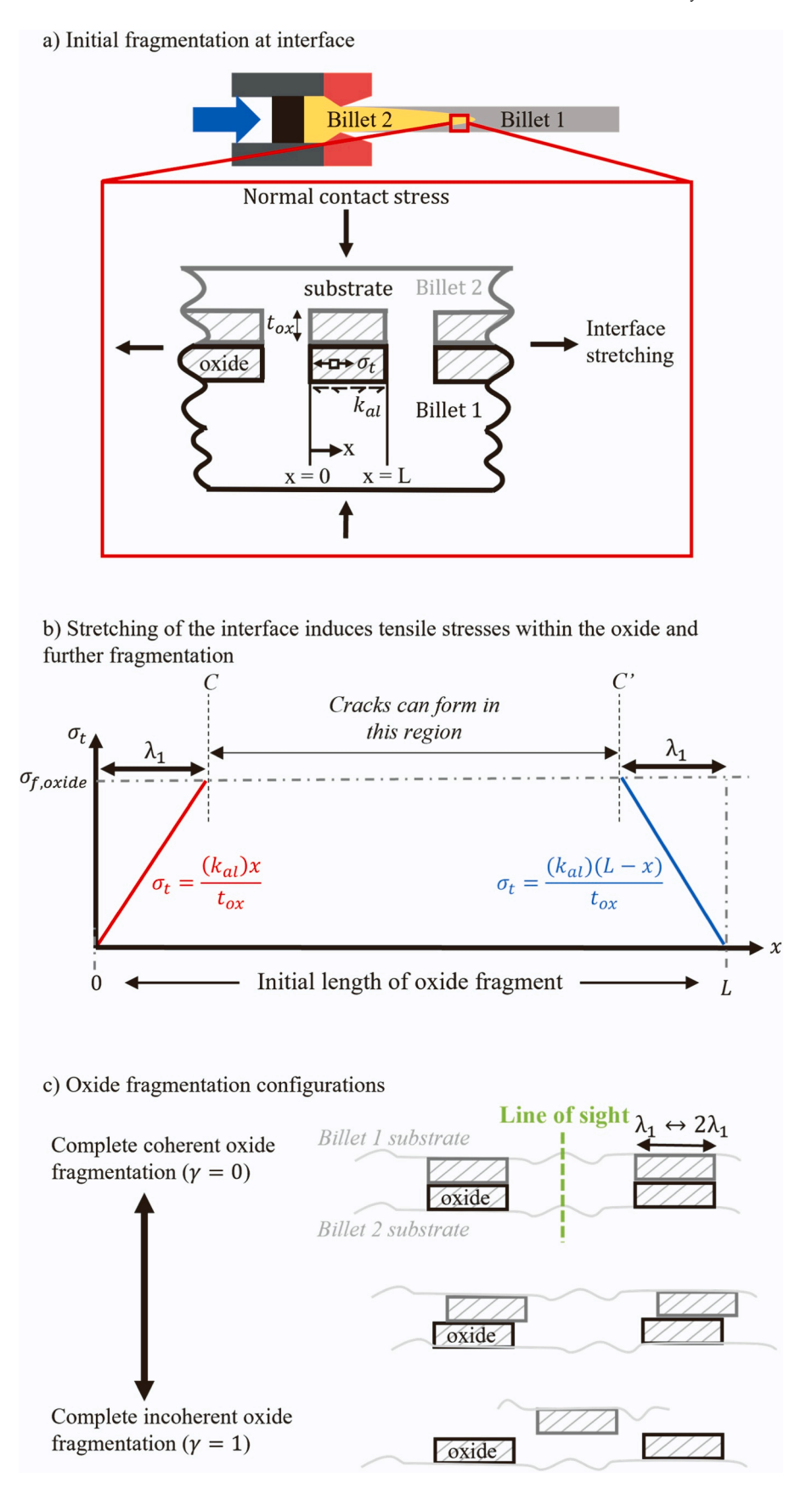


Fig. 3. Shear lag modeling of oxide fragmentation at the billet-billet interface. Final oxide fragment lengths are expected to vary from to λ_1 to $2\lambda_1$.

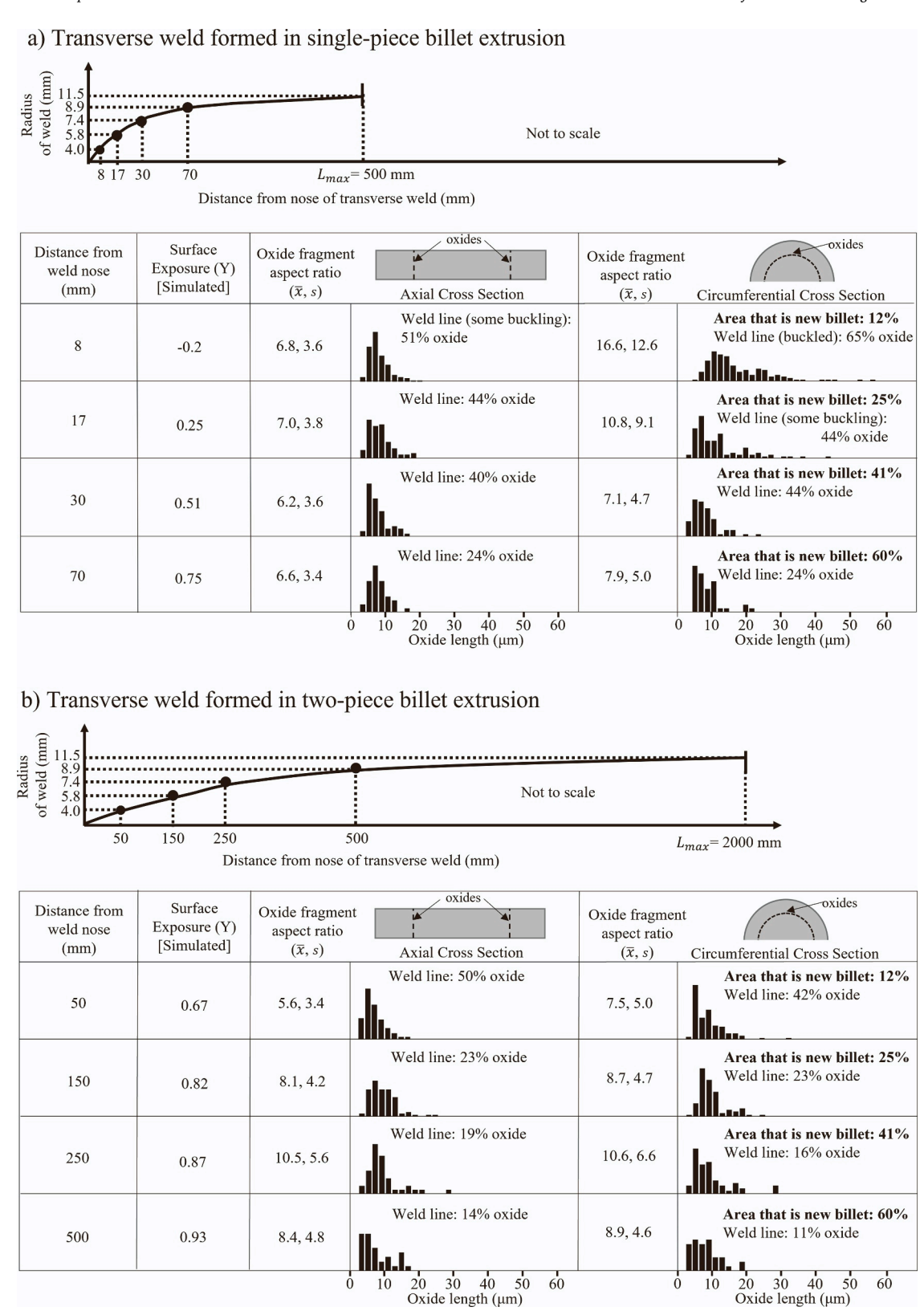


Fig. 4. Experimentally observed oxide fragmentation of 0.9 μm anodized billets in (a) single-piece and (b) two-piece billet extrusion. Weld line % oxide is total length of observed oxide along weld line (irrespective of fragmentation mode) divided by the straight line or circular weld length. It is not indicative of weld area % oxide in cases of interface buckling.

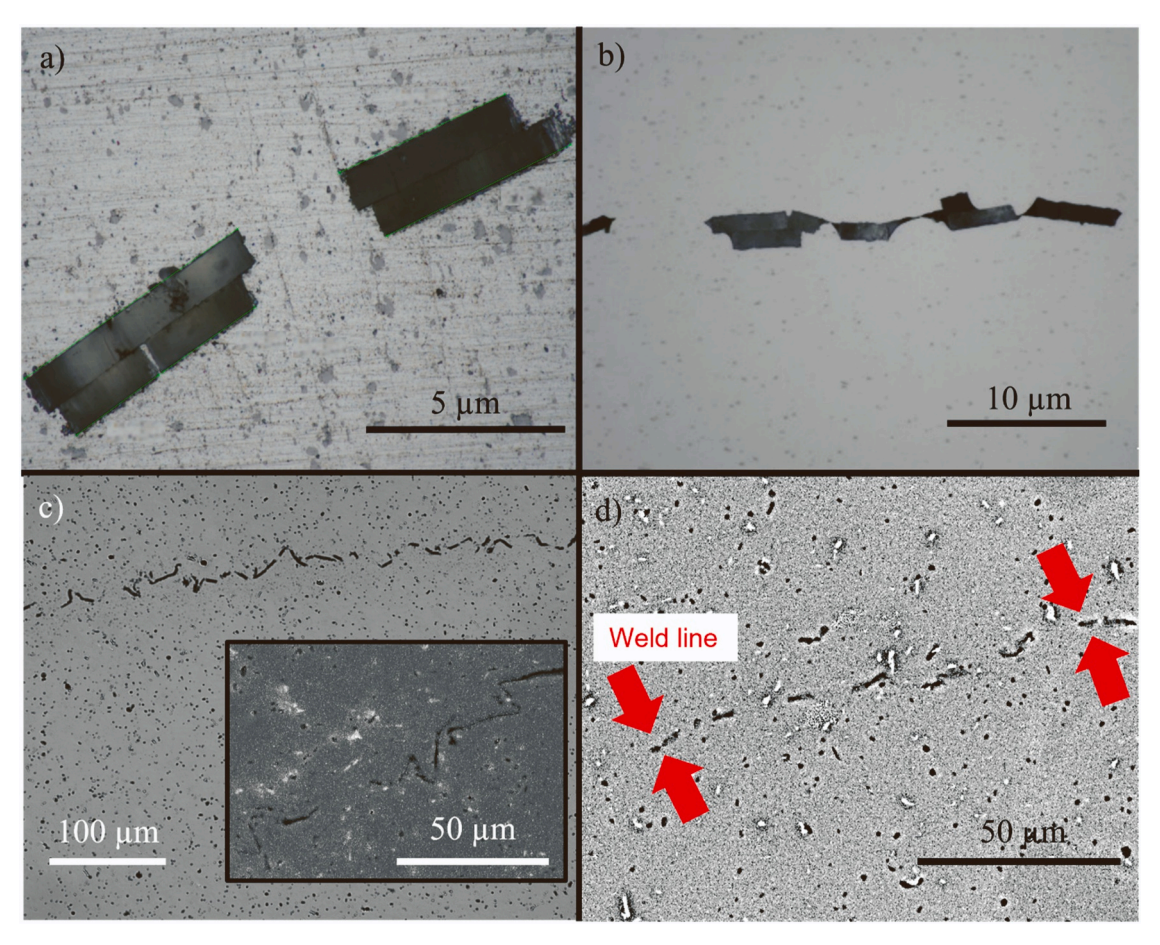


Fig. 5. Microscopy of circumferential oxide fragmentation for single-piece billet extrusion. (a) Optical microscopy showing (near complete) coherent oxide fragmentation. (b) Optical microscopy showing incoherent oxide fragmentation. (c) Optical and SEM (inset) of the weld nose (12% new billet). (d) SEM of oxides at 41% new billet.

2.2.1. Calculating the exposed aluminum substrate area fraction (ν)

The exposed substrate area ($A_{exposed}$) is equal to the interface area ($A_{nominal}$), less the original area covered by oxides ($A_{original}$), less the area of exposed substrate oxidized by entrapped air ($\eta A_{original}$), and less the increase in interface area needed to create line-of-sight substrate-to-substrate channels through the cracks in the oxide layers ($\gamma A_{original}$). The fraction (ν) of the interface area that is exposed substrate is therefore given by Eq. 4, which can be rewritten as Eq. 5, eliminating the area terms by introducing the surface exposure, γ .

$$\nu = A_{exposed} / A_{nominal} \Rightarrow \nu = \left[A_{nominal} - A_{original} (1 + \eta + \gamma) \right] / A_{nominal}$$
(4)

$$\therefore \nu_{transverse} = Y + (\eta + \gamma)(Y - 1)$$
weld (5)

where Y is the interface surface exposure, η is the fractional surface area expansion that is oxidized due to entrapped air, and γ is the fractional increase in the original interface area needed to create line-of-sight substrate-to-substrate channels through the cracks in the oxides. Each parameter is described below.

The surface exposure (Y) has been used previously in the roll bonding literature (e.g., Bay, 1983) and is defined as the difference between the current interface area ($A_{nominal}$) and the original interface area ($A_{original}$) divided by the current interface area (Eq. 6).

$$Y = \frac{A_{nominal} - A_{original}}{A} \tag{6}$$

For uniaxial stretching of the interface (as in rolling), $Y_{plane} = \frac{e^{mg}}{1 + e^{mg}}$

In Eq. 7, the calculation is rewritten for the case of a biaxial strain state as exists in transverse weld formation. Eq. 7 is derived by considering the deformation of an infinitesimal square on the interface that is subjected to perpendicular in-plane strains, ε_1 and ε_2 .

$$Y_{transverse} = 1 - 1 / [(1 + \varepsilon_1^{eng})(1 + \varepsilon_2^{eng})] = 1 - \exp[-\varepsilon_1^{arue} + \varepsilon_2^{true})]$$
 (7)

Cooper and Allwood (2014a) argue that the significant threshold deformation needed for welding to occur in roll bonding is due to entrapped air oxidizing initially exposed substrate. They estimate the moles of entrapped oxygen at the interface by considering the air temperature and interface surface roughness. They then estimate the area of exposed substrate aluminum these moles of oxygen will oxidize; thus, deriving an estimate for the fractional increase in interface area (η , Eq. 8) needed before any further expansion of the interface occurs in an inert atmosphere.

$$\eta = \frac{A_{oxidation\ limit} - A_{original}}{A_{original}} \approx 50000 \times \sqrt{2}r \times cosine(\sqrt{2}\psi) \times \frac{298}{T}$$
 (8)

where r is the surface root mean square asperity height, in meters, ψ is the asperity inclination angle, and T is the bonding temperature, in Kelvin. The calculation of η for transverse weld formation remains unchanged from the original C-A model.

The γ parameter is introduced to model the effect of coherent versus incoherent oxide fragmentation (Fig. 3c). $\gamma=0$ for complete coherent fragmentation, as the layers of broken oxide on opposite sides of the interface cover the same regions of substrate. $\gamma=1$ for complete

incoherent fragmentation, as at the limit the original interface area doubles and misalignment of the oxide layers still prevents line-of-sight substrate-to-substrate channels across the interface. A mix of fragmentation modes occur in extrusion (Assumption C). The problem is bounded by using $\gamma = 0 \leftrightarrow 1$.

For any welding to occur, the local contact area must expand (Assumption D) and substrate-to-substrate channels across the interface be created, $\nu > 0$. Therefore, a threshold minimum surface exposure, Y', is required. Y' is defined in Eq. 9 and derived by setting Eq. 5 to zero.

$$Y' = (\eta + \gamma)/(1 + \eta + \gamma) \tag{9}$$

2.2.2. Calculating the minimum micro-extrusion normal contact stress (p_{ex}) The minimum normal contact stress needed to micro-extrude substrate aluminum through cracks in the billet-billet oxide layers depends on the geometry of the exposed substrate and oxide fragments. An idealized repeating unit cell (Fig. 6a) is considered at the billet-billet

interface. The unit cell contains exposed substrate and the corners of four equally spaced, equally sized, oxide fragments (Assumptions A and B).

The mean oxide fragment length ($\lambda_{Average}$) for native oxides $(t_{oxide} \approx 4nm)$ is approximated using shear lag modeling (Assumption A). For example, using Eq. 3, for AA6061 extruded at 425 °C ($k_{Al} \approx 40MPa$), $\lambda_{Average} \approx 36nm$. Eq. 10 defines the area of the unit cell ($A_{unit\ cell}$). The $(1+\eta)$ term accounts for the oxides observed in the unit cell being the result of both the original oxide film and newly oxidized exposed substrate. Inclusion of the surface exposure (Y) in Eq. 10 comes from $A_{unit cell}$ being equivalent to $A_{nominal}$ in Eq. 6.

$$A_{unit\ cell} = A_{original} / (1 - Y) \approx \frac{\lambda_{Avg}^2}{(1 + \eta)(1 - Y)}$$

$$\tag{10}$$

The area of exposed substrate in the unit cell (A $_{exposed,}$) is given by Eq.

11 and is equal to the area of the unit cell (Eq. 10) less the projected area of oxide in the unit cell. For $\gamma = 0$, this area of oxide is λ_{Avg}^2 . Eq. 11 can be used to calculate the minimum surface exposure needed for the exposed substrate area in the unit cell to be positive. This results in the same threshold minimum surface exposure as calculated in Eq. 9, confirming model consistency across the new calculations of ν and p_{ex} .

$$A_{\substack{exposed, \\ write cell'}} \approx \max \left(\frac{\lambda_{Avg}^2}{(1+\eta)(1-Y)} - \frac{\lambda_{Avg}^2(1+\eta+\gamma)}{(1+\eta)}, 0 \right)$$
 (11)

Using Eqs. 10 and 11, an expression for the micro-extrusion pressure, p_{ex} , is derived using classic equilibrium extrusion analysis (Saha, 2000).

 p_{ex} is assumed equal to the extrusion pressure needed in axisymmetric extrusion of a round billet of cross-sectional area, Aunit cell, into a round rod of cross-sectional area, $A_{exposed.}$, using dies with a land length of t_{oxide}

and a dead zone angle of 90°. While a crude assumption, the results in Section 4 show that in hot extrusion the modeled transverse weld strength results are likely insensitive to small variations in the estimate of p_{ex} . Eq. 12 shows the new expression for the micro-extrusion pressure, p_{ex} . The first term derives from the pressure needed to deform the substrate through the gap in the oxides and the second term derives from the pressure needed to overcome the sticking friction shear stresses along the walls of the oxide fragments. ER is the micro-extrusion ratio for the unit cell (Eq. 14), calculated using Eqs. 10 and 11. Fig. 6b shows some typical results for p_{ex} using Eq. 12. Fig. 6b shows that the initially high values of p_{ex} are sharply reduced as the surface exposure increases. A more sophisticated analysis could replace the assumption of a single value for the oxide fracture strength and a single value for the oxide thickness with a statistical approach to reflect the uncertainty in these values. However, even significant variations in these parameters have only a modest effect on the calculated micro-extrusion pressure and therefore the calculated weld strength. For example, in reference to Fig. 6b ($\eta = \gamma = 0$), at a surface exposure (Y) of 0.4 then a 50% increase in oxide thickness (to 6 nm) only increases the micro-extrusion pressure (p_{ex}) by 6% from 71 MPa to 75 MPa. Similarly, changing the oxide fracture strength by \pm 50% only changes the p_{ex} by \pm 3%.

$$p_{ex, trans. weld} \approx \sigma_{flow} \ln(ER) + 2.t_{oxide} \cdot \sigma_{flow} \cdot \left(\frac{\pi}{3.ER.A_{unit cell}}\right)^{0.5}$$
 (12)

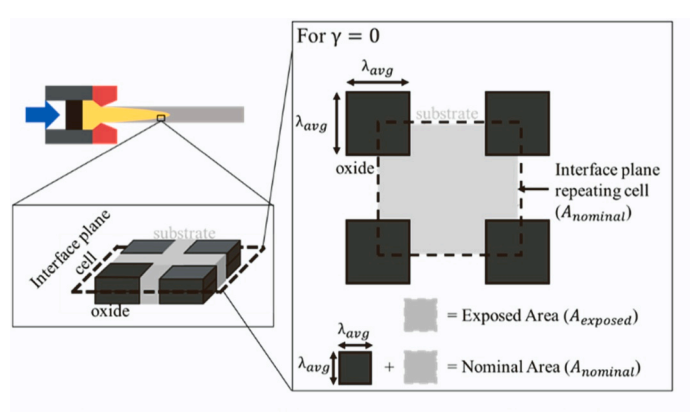
$$ER = A_{unit \ cell} / A_{\substack{exposed, \\ unit \ cell}}$$
(13)

$$\therefore ER = 1/[Y(1+\eta+\gamma) - (\gamma+\eta)]$$
 (14)

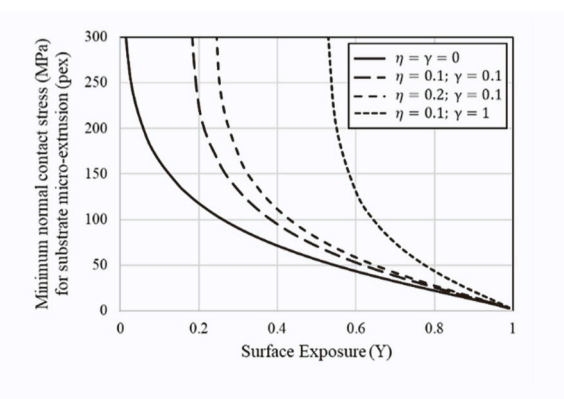
2.3. Calculating the local transverse weld strength

In summary, the following calculation updates have been made to the C-A model:

- The fraction of the interface that is exposed substrate (ν) has been revised (Eq. 5) to include an oxide fragmentation coherency parameter (γ) .
- The surface exposure (Y) has been defined (Eq. 7) for an in-weldingplane biaxial strain state.



a) Schematic of the modeled repeating unit cell at the local billet-billet interface



b) P_{ex} results using equation 12. Modeled for $\sigma_{flow} =$ 70 Mpa, $t_{oxide} = 4$ nm, and $\lambda_{Average} = 36$ nm

Fig. 6. Calculating the minimum micro-extrusion pressure (p_{ex}) .

 The minimum micro-extrusion normal contact stress (p_{ex}) has been revised (Eq. 12) to account for biaxial oxide fragmentation at the welding interface.

With these updates to the C-A model inputs, Eq. 1 can be used to predict the local transverse weld strength. This is achieved by tracing the deformation conditions experienced at points on the original planar billet-billet interface along streamlines through the extrusion die to their final position in the extruded profile. τ_b (Eq. 1) is evaluated along the streamlines for each point (see Fig. 7). As no regions of hydrostatic tension exist along the evolving interface, it is assumed that the local weld strength can only increase and is equal to the maximum realization of Eq. 1 anywhere along the streamline.

3. Methodology for evaluating the new transverse weld strength model

A series of extrusion trials are conducted (Section 3.1) and the strength of the generated transverse welds evaluated using shear tests (Section 3.2). The experimental weld strengths are then compared to predictions made using the new model. The model inputs are extracted from finite element models (FEM) of the extrusion trials (Section 3.3).

3.1. Extrusion trials and alloys

Three profiles are extruded using different alloys and presses to test model flexibility. Table 1 presents the profiles, die geometries, and extrusion settings. Fig. 8 presents the flow curves (σ_{flow}) for the aluminum alloys. A high-resolution AA6082 flow curve model is provided by DEFORM (sourced from Heinemann, 1961), and the AA6061 flow curves are sourced from Ding et al. (2021). The compositions of the alloys are shown in Table 2. Tabulated flow stress data from Fig. 8 (as a function of strain, strain rate, and temperature) are used as the DEFORM material model inputs. This is DEFORM's recommended method of describing material response rather than inputting estimated constitutive equation parameters. DEFORM then uses linear interpolation in the log-log space in order to calculate flow stress values across the strain-strain rate-temperature parameter space.

3.2. Evaluating the experimental weld strengths

Room temperature shear tests (1 mm/minute crosshead displacement) were conducted on samples extracted from the axisymmetric and rectangular profiles. In all cases, wire electrical discharge machining (EDM) was used to produce shear test geometries that isolate the weld in the test region (see Fig. 9).

The shear test sample geometries (Fig. 9c) are modified from the ASTM B831–05 standard (ASTM, 2010) to have a wider test region so as to reliably incorporate the transverse weld. The modified shape is similar to the shear test sample geometry suggested by Merklein and Biasutti (2011) to facilitate fatigue shear testing and shown by Yin et al. (2014) to experience a similar strain distribution to the ASTM standard.

Reductions in sample geometry were necessary to test the strength of welds at the rear of the profile. In all cases, shear testing of the adjacent bulk material using identical shear test geometries was performed to calibrate the results.

For non-axisymmetric profiles, local deformation conditions at the weld vary across as well as along the profile. For the rectangular bar, test samples were extracted from both the major and minor axis of the ellipsoid shaped weld. It was impractical to test directly the strength of the multi-nose weld created in the hollow profile. Therefore, the visibility of the weld across etched cross-sections was used instead as a proxy for the strength, as used in other aluminum extrusion weld studies (e.g., Kolpak et al., 2019).

3.3. Determining model inputs

The derived model for the local transverse weld strength is a function of the key extrusion process parameters: the billet material properties, extrusion temperature, ram speed, and the geometry of the container and die (e.g., extrusion ratio). Some of these parameters (e.g., ram speed) are not direct inputs in Eq. 1 but are represented in the calculation of the other inputs (e.g., σ_n and p_{ex}) derived from a FEM of the extrusion process. For example, changes to the extrusion ratio will, via the FEM, change the biaxial strain state at the weld interface and therefore the fraction (ν) of the interface area that is exposed substrate. Similarly, changes to the ram speed will affect the strain rate and therefore the local stress state (σ_n and τ) as well as the billet flow stress (σ_{flow} , via the material model) and therefore the minimum normal contact stress (p_{ex}) required for substrate micro-extrusion.

3.3.1. Finite element models

The extrusion trials listed in Table 1 were simulated using DEFORM® software. The FEMs were run using the multifrontal massively parallel sparse direct solver and the Newton-Raphson iteration method. The billets were modeled as von Mises materials with isotropic hardening and different flow curves used for different temperatures and strain rates (Fig. 8). The die, container, and dummy block were modeled as rigid bodies. Contact between the billet-die and billet-container were modeled using sticking friction (a friction coefficient of m = 1 where the frictional shear stress, $\tau = mk$, and k is the aluminum billet shear yield stress), and between the billet-dummy block as frictionless (m = 0), reflecting the use of boron nitride lubricant on the dummy block. While the actual friction coefficient between the dummy block and billet is non-zero, the impact of assuming frictionless billet-dummy block contact is negligible as determination of the ram force is instead dominated by the billet material properties, die shape, and the friction condition between the billet and container. In addition, Hatzenbichler and Buchmayr (2010) found the transverse weld geometry is unaffected by the friction conditions between the billet and dummy block. In the extrusion FEMs, the typical element size was $\approx 0.75 \text{ mm}$ in the die region and $\approx 1.5 \text{ mm}$ elsewhere. Remeshing occurred when the billet-tooling interference exceeded 0.25 mm. An axisymmetric model was used to simulate extrusion of the round rod. A quarter-size symmetric 3D model

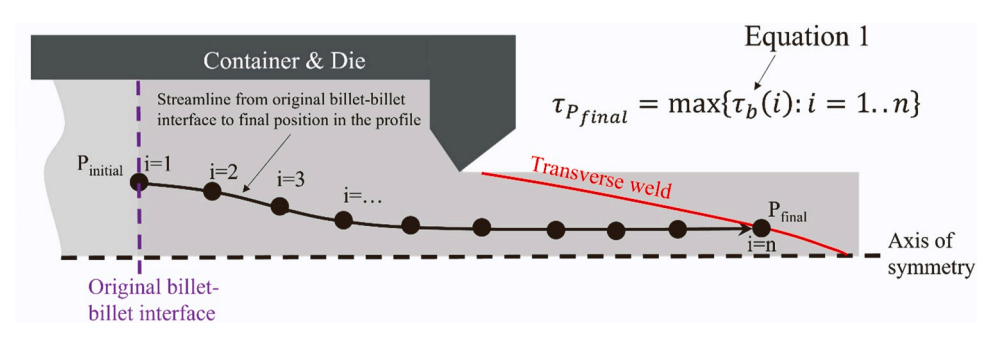


Fig. 7. Implementation of the new transverse weld strength model.

 Table 1

 Details of the experimental extrusion trials performed in this work. Note: One set of axisymmetric single-piece billet experiments tested extrusion without use of the butt shear.

Profile	Round rod	Rectangular bar	Hollow		
Profile image	1 <u>0 m</u> m	10 <u>m</u> m	10 <u>m</u> m		
Profile dimensions (mm)	Ø23.08	6.06 x 60.6	26 x 142 outer dimensions		
Alloy	AA6061	AA6061	AA6082		
Die image	Container side	Container side	Container side (8 die ports)		
Tongue-shaped weld geometry (generated from FEM; colors are for visualization purposes only)					
Billet diameter (mm)	Ø88.9 (3.5")	Ø152.4 (6")	Ø228.6 (9'')		
Billet length (mm)	1x203.2 (8") for single- piece billet extrusion 2x101.6 (4") for two- piece billet extrusion	800 (31.5") Single-piece billet extrusion	1120 (44") Single-piece billet extrusion		
Extrusion ratio	15	50	26		
Ram speed (mm/s)	1.0	5.6	4.7		
Billet temperature (°C)	425	450	493		

was used to simulate extrusion of the rectangular bar, and a full 3D model was used to simulate extrusion of the complex asymmetric hollow profile.

The accuracy of the FEM simulations was ensured by performing several checks. A mesh refinement study ensured sufficient mesh density for accurate prediction of the ram force and the weld geometry. The ram force and new billet area predictions were within \pm 10% of the experimentally measured forces and new billet areas (determined by sectioning and etching the profiles). Fig. 10 shows a comparison

between the simulated and measured weld geometries. In order to determine the experimental weld geometries in Fig. 10, a series of cross-sectional samples were cut from along the extruded profiles. These samples were etched in a 10% sodium hydroxide solution heated to 100 $^{\circ}\text{C}$ for 15 min. The samples were then rinsed in deionized water, dipped in nitric acid to clean the etching residue, and then rinsed in deionized water once more. The samples were then imaged on a Nikon AZ100 microscope with a low optical zoom and then characterized using IC measure computer software. The position of the weld nose was found

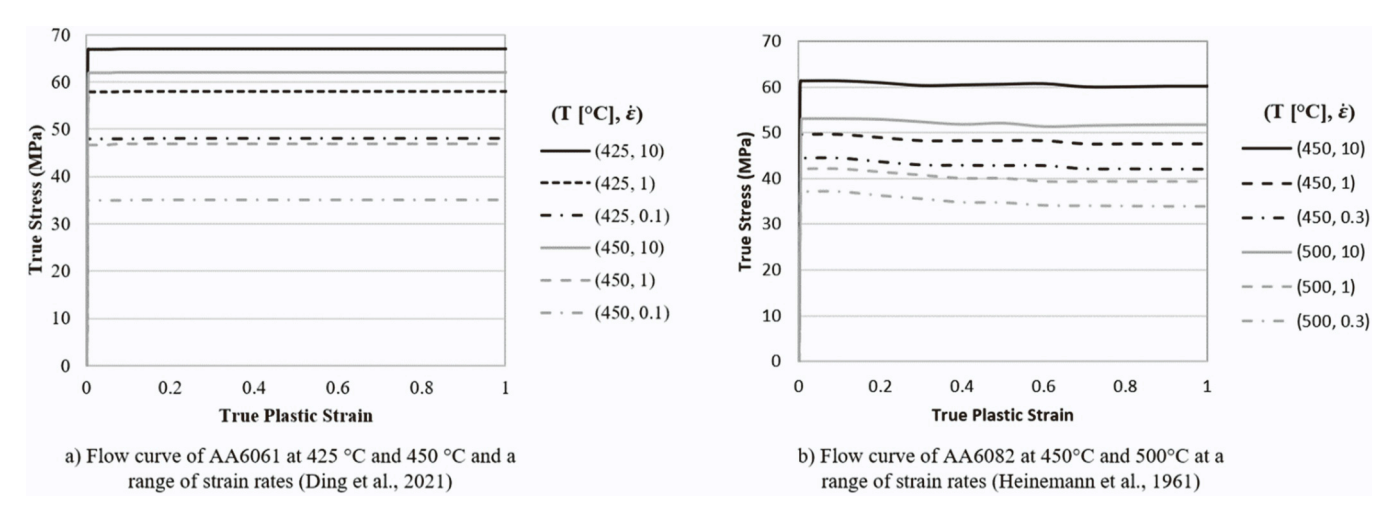


Fig. 8. Flow curves for the aluminum alloys used in the extrusion trials.

 Table 2

 Composition of the aluminum billets used in the trials.

Alloy Designation	Element composition (weight %)*											
	Si	Fe	Cu	Mn	Mg	Cr	Zn	Ti	Pb	Other		
										Each	Total	
6061 6082	0.4–0.8 0.7–1.3	0.7 0.5	0.15–0.4 0.1	0.15 0.4–1.0	0.8–1.2 0.6–1.2	0.04–0.35 0.25	0.25 0.2	0.15 0.10	0.003 0.003	0.05 0.05	0.15 0.15	

The remainder is aluminum. Values refer to the composition maximum unless shown as a range.

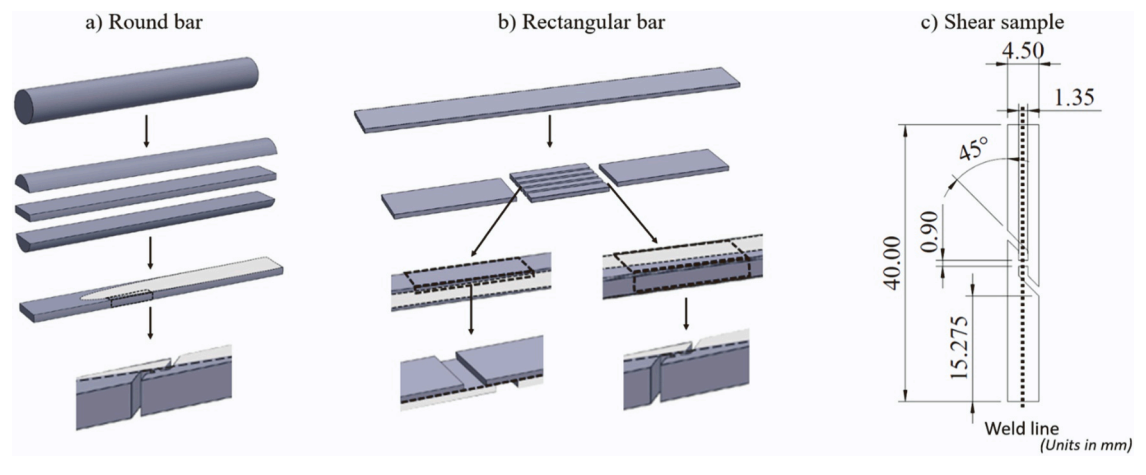


Fig. 9. Shear test sample machining process using wire EDM.

experimentally by taking cross-sectional cuts every few millimetres in the region of the profile deemed by the simulation work to likely contain the nose. Note that to produce Fig. 10e (simulation), the velocity field from the DEFORM post-processor was extracted and then a simple MATLAB script used to track a plane of points corresponding to the original billet-billet interface through the die. This results in a 3d point cloud with the points positioned across and along the weld shape within the profile. To produce a cross-sectional view of the weld at any given axial position from the nose, the point cloud between that position and the nose is projected onto the 2d cross-section.

3.3.2. Model inputs: Evolving deformation conditions at the billet-billet interface $(\sigma_n, \tau, \varepsilon_1, \varepsilon_2)$

To implement the new model (Fig. 7), the normal contact stress, shear stress, and surface strains must be determined along streamlines of

material from the initially planar billet-billet interface through the die to the final point on the profile weld. DEFORM®'s point tracking feature is used to track the displacement and global stress tensor (σ_t) of a particle as it flows along its streamline. For a given particle of interest (c_1) on the initial planar billet-billet interface, the displacements are tracked of two adjacent particles $(c_2$ and $c_3)$ that also lie on the interface and are initially a small distance from c_1 such that the vector $c_{1\rightarrow 2}$ is perpendicular to $c_{1\rightarrow 3}$. The local unit normal (\widehat{n}_t) to the interface at any time, t, is determined by normalizing the cross product of $c_{1\rightarrow 2,t}$ and $c_{1\rightarrow 3,t}$. The evolving local traction vector along the streamline $(T_t, \text{Fig. 11})$ is then calculated according to Eq. 15.

$$T_t = \sigma_t \hat{n}_t \tag{15}$$

The local normal contact stress (σ_n , Eq. 16) and shear stress (τ , Eq. 17) are then defined using the axioms of stress analysis.

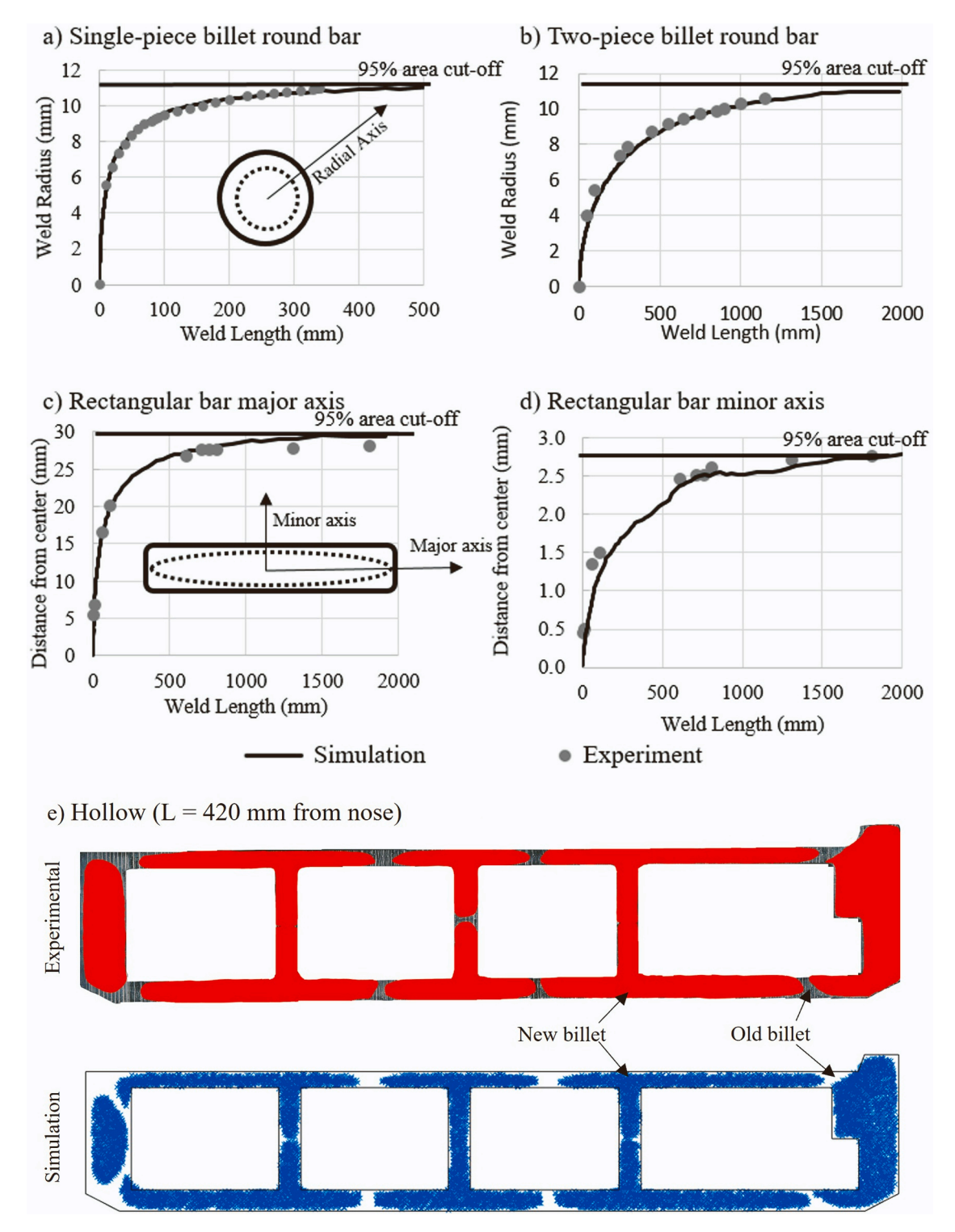


Fig. 10. Comparison of experimental and simulated weld geometries.

$$\sigma_{n,t} = T_t \bullet \widehat{n}_t \tag{16}$$

$$\tau_{t} = \sqrt{\|T_{t}\|^{2} - \sigma_{n,t}^{2}} \tag{17}$$

Eqs. 18 and 19 define the perpendicular surface strains experienced in the small region around the particle of interest. These strains are estimated by tracking the relative displacement of the adjacent particles and applying the definition of engineering strain as change in length divided by original length.

$$\varepsilon_{1,t}^{eng} \approx \left[\| c_{1\to 2,t} \| - \| c_{1\to 2,t=0} \| \right] / \left[\| c_{1\to 2,t=0} \| \right]$$
(18)

$$\varepsilon_{2,\perp 1,t}^{eng} \approx \left[\left\| c_{1\to 3,t} \times \frac{c_{1\to 2,t}}{\|c_{1\to 2,t}\|} \right\| - \left\| c_{1\to 3,t=0} \right\| \right] / \left[\left\| c_{1\to 3,t=0} \right\| \right]$$
 (19)

3.3.3. Other model inputs (η and Y')

Eq. 8 is used to calculate the fractional increase in interface area (η) needed for further expansion to occur in an inert atmosphere. The root

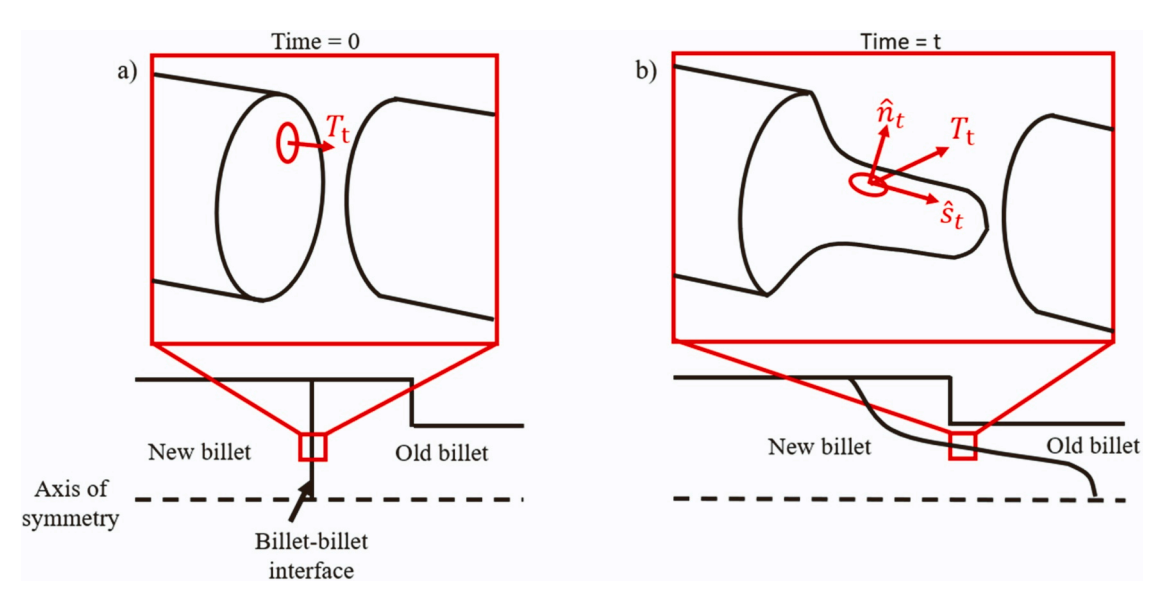


Fig. 11. DEFORM® simulation output is used to calculate the local traction vector (T_t) and unit normal vector (\hat{n}_t) .

mean square asperity height, r, was determined using an AMTAST portable surface roughness tester for the billets used in the round profile $(r=0.3~\mu\text{m})$, rectangular bar $(r=7.5~\mu\text{m})$, and complex hollow profiles $(r=7.5~\mu\text{m})$. A typical asperity inclination angle $(\psi\approx 6^\circ)$ for machined surfaces was also used (Grigoriev, 2015), resulting in η values ranging from 0.01 (round bar profile) to 0.20 (rectangular bar profile). Using Eq. 9, these η values translate into threshold minimum surface exposure, Y', values ranging from 0.01 for the round bar to 0.17 for the rectangular bar profile (evaluated for $\gamma=0$).

3.4. Model implementation

Fig. 12 shows how the key deformation conditions are tracked along streamlines of material for two points on the mid-plane of the rectangular bar profile. Fig. 12 (top) shows how the surface exposures and normal contact stresses vary from the initial planar billet-billet interface to die exit. It shows that points near the weld nose (e.g., RA) experience negative surface exposures ($\nu = 0$) and are therefore predicted to have a zero weld strength. For point RB, Fig. 12 shows the normal contact stress is highest at the start when the interface unit normal is parallel with the extrusion direction. However, the local surface exposure at the start is lower than the threshold value (Y') needed to expose reactive substrate aluminum; therefore, no welding can occur initially. Once the surface exposures exceed the threshold (at $Z\approx 12$ mm), the pressure needed for substrate micro-extrusion through the oxide cracks (p_{ex}) quickly drops to below the actual normal contact stress, σ_n . Thus, welding can occur between $Z \approx 12$ mm and $Z \approx 48$ mm, which corresponds to the die exit when σ_n drops below p_{ex} . For point RB, the maximum realization of Eq. 1 occurs just before the die exit, at $\tau_b = 0.71 \times \tau_o$.

4. Results: Experimental and modeled weld strengths

4.1. Weld strengths in the round rod and rectangular bar

Fig. 13 presents experimental and predicted transverse weld strengths (y-axis) as a function of the axial distance from the weld nose (x-axis). The weld shear strengths are expressed as a percentage of the bulk material shear strength.

The experimental results show several trends including a positive correlation between increasing distance from the nose and the weld strength. Figs. 13a and 13b show that two-piece billet welds, despite being longer than single-piece equivalents, experience a similar rise in weld strength with distance from the weld nose. Many two-piece billet

transverse weld samples reach bulk metal strength long before the end of the 2 m weld. Fig. 13a also shows that consecutive extrusion of singlepiece billets without the use of a butt shear has a deleterious effect on the weld strength. The front 10 cm of these welds break apart on attempts to machine a sample. This weakness is likely due to lubricant on the back of the previously extruded billet (transferred from the dummy block) and potentially contaminants in the (unremoved) back-end defect. Lubricants minimize the frictional restraint against incoherent oxide cracking. More importantly, lubricants themselves wet the interface and form a physical barrier to substrate-on-substrate contact. The lubricant was likely squeezed towards the billet center as normal contact stresses are highest on the outside of the billet-billet interface (Fig. 12). Consistently, Fig. 13a shows negligible strength for the first 200 mm from the nose and then a sudden increase to close to 100% of the bulk strength at the weld rear, corresponding to the outside of the billet. Figs. 13c and 13d show that for the rectangular bar, the weld strength of samples extracted from along the minor axis of the ellipsoid shaped weld are greater than those of samples extracted from along the major axis. One tested sample from along the minor axis displays bulk metal shear strength.

The model predictions in Fig. 13 are shown bound by assumptions of complete coherent and incoherent oxide fragmentation ($\gamma = 0$ –1). There are areas of disagreement between the predictions and experimental results; for example, the model over-predicts the weld strength near the nose along the minor axis of the ellipsoid shaped transverse weld in the rectangular bar profile (Fig. 13d). Nonetheless, the model can be used to help explain the experimental results. Fig. 14 shows the surface exposure and stress histories along material streamlines for points on the round rod and rectangular bar transverse welds. Fig. 14a and b show that the size of the region where welding is possible gets smaller towards the nose of the weld as does the final value of the surface exposure. For the case of point 1 A, located near the center of a single-piece billet, surface exposures are negative and no welding is predicted. In contrast, for point 2 A, located near the center of a two-piece billet, surface exposures are significant by die exit ($Y \approx 0.4$) and welding is predicted. In Fig. 14, whenever Y > Y', the normal contact stress (σ_n) quickly exceeds the minimum micro-extrusion pressure needed for substrate-on-substrate contact (p_{ex}) and bonding is predicted to occur. Fig. 14c shows that at the same axial position in the rectangular bar profile, a point placed on the minor axis (RBy) experiences a greater surface exposure (and therefore a higher predicted weld strength) than a point placed on the major axis (RBx).

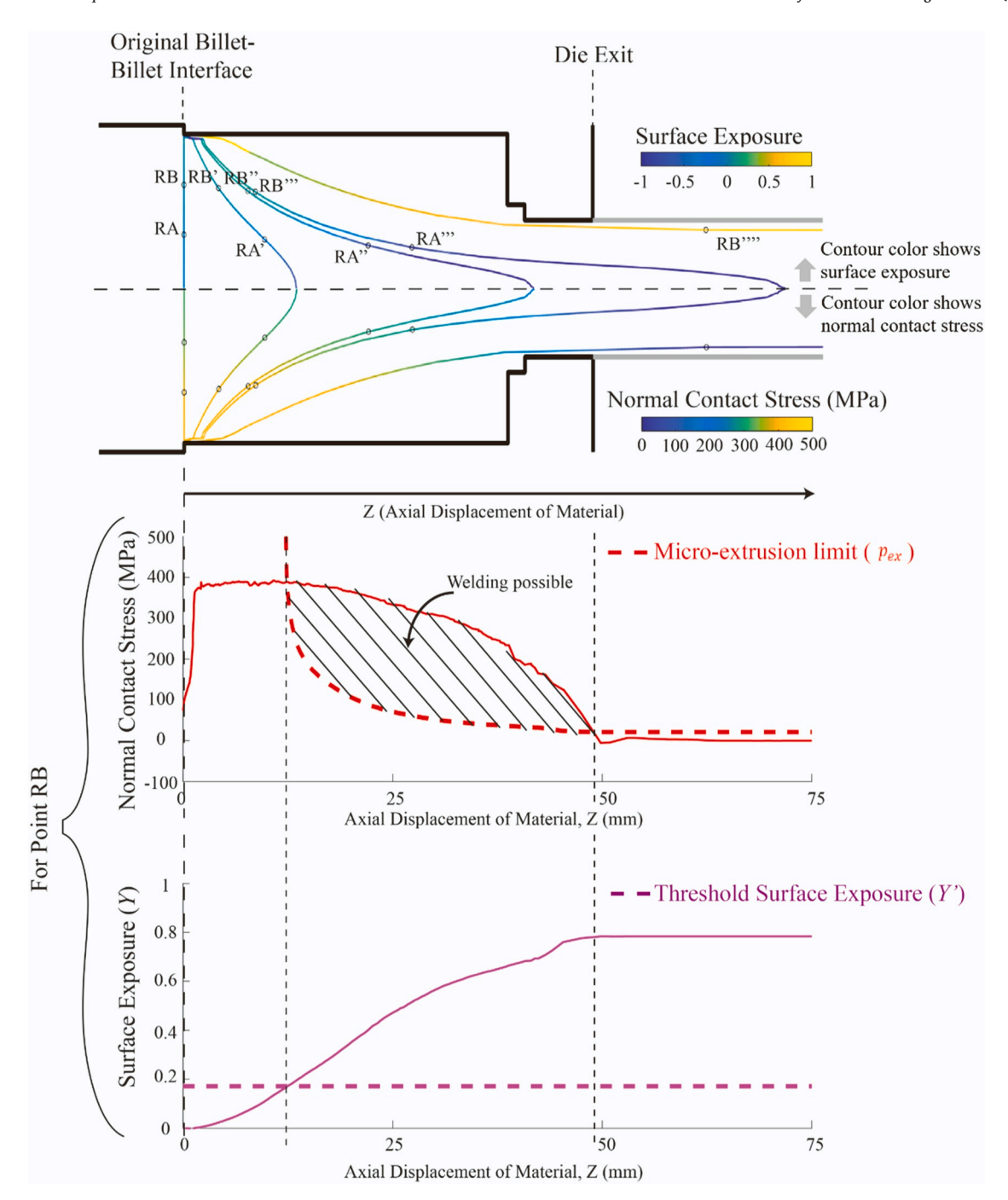


Fig. 12. Tracking the deformation conditions across the major axis plane on the billet-billet interface during extrusion of the rectangular bar. Modeled for $\gamma=0$.

4.2. Weld strengths in the complex hollow extrusion

Fig. 15 shows the model weld strength predictions and the experimental weld visibility across cross-sections near the front, middle, and rear of the weld. This profile contains eight tongue-shaped welds corresponding to each die port. The weld noses are not aligned axially: the weld nose corresponding to the right-hand side of the cross-section (as viewed in Fig. 15) is \approx 200 mm further forward into the profile than the weld nose on the left-hand side. Fig. 15 (right) shows high weld visibility around the nose of each weld. In addition, the weld is most visible in high curvature regions of the weld line (disappearing in the flatter portions), which is consistent with the weaker weld strengths seen along the major (high curvature) axis in the rectangular bar (Fig. 13c). Fig. 15 (left) shows the modeled weld shear strength evaluated over the

complex 8-tongue weld geometry. Using weld visibility as a proxy for strength, the model correctly predicts high visibility near each of the weld noses, the higher visibility around high curvature regions of the weld, and lower visibility on flat regions both near and far from the nose.

4.3. Weld fracture morphology

Fig. 16 shows fracture surfaces for samples extracted from weak and strong welds. These images are representative of the fracture surfaces found across the profiles. The fracture surface created by breaking the strong weld shows long, drawn out tongue-shaped fragments around $10~\mu m$ in length, which were likely formed as the weld plastically deformed in the shear test direction. In contrast, the fracture surface created by breaking the weak weld is relatively planar with small thorn-

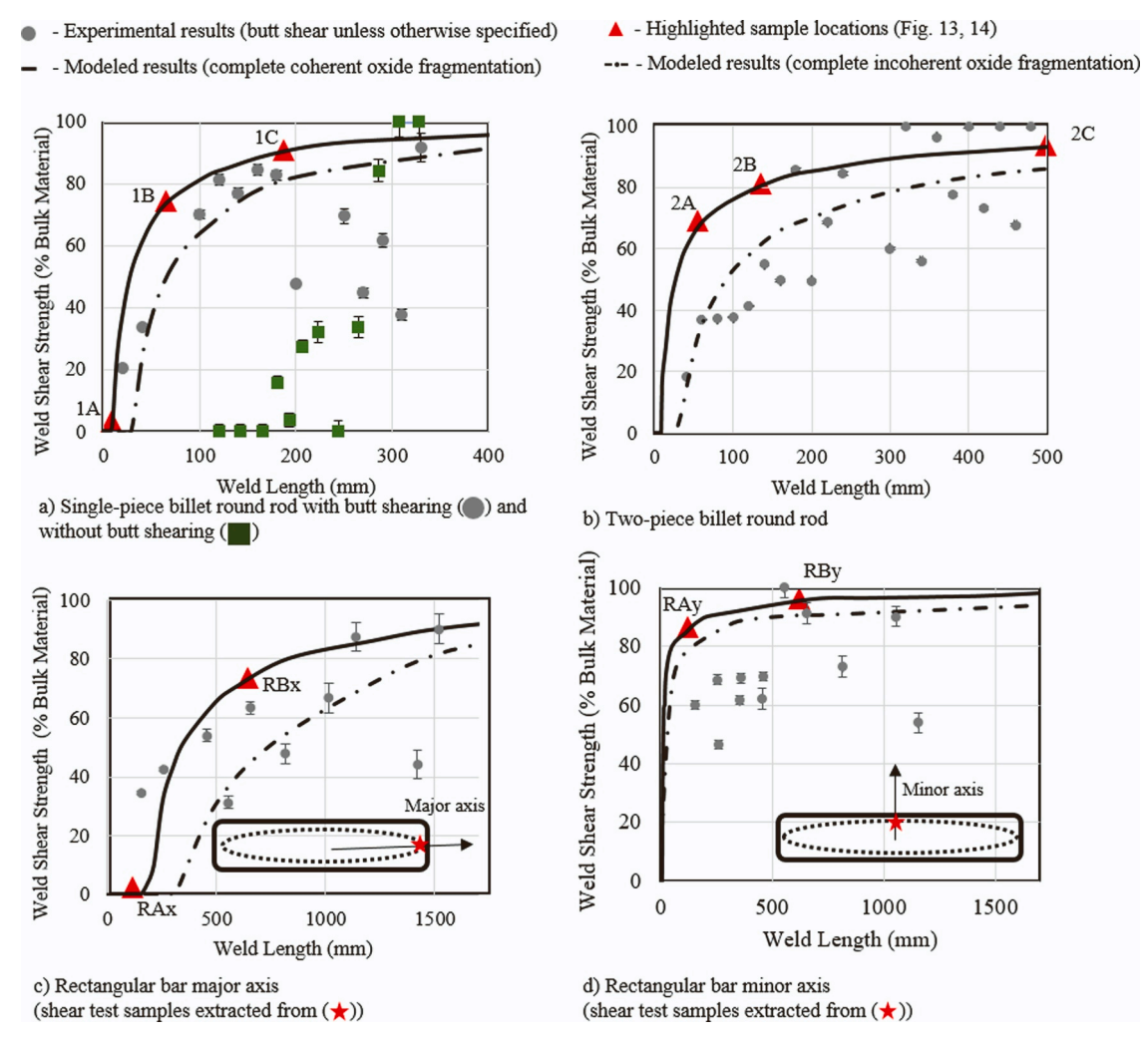


Fig. 13. Experimental and modeled aluminum extrusion transverse weld strengths for the AA6061 round bar and rectangular bar profiles.

shaped fragments orientated in the shear test direction which are less than $1~\mu m$ in length, suggesting brittle failure.

4.4. Sources of error

The main error in the experimental determination of the weld shear strength is uncertainty in the fracture area measurement. The thicknesses of the shear test samples were measured using a micrometer and the length of the fracture region measured using a low-zoom microscope. For each measurement, an uncertainty of \pm 0.1 mm is assigned. This translates to a strength calculation error of \pm 0.6% for the largest test geometries (near the weld nose) and \pm 5% for the smallest test geometries needed towards the weld rear. Potential damage to the welds caused by the EDM process is another potential source of error.

Parametric uncertainty is estimated to translate to $\pm\,10\%$ uncertainty in the modeled strength predictions. This uncertainty originates from imperfect material specifications (e.g., billet flow curves), an experimental uncertainty of $\pm\,2$ mm in the original position of the planar billet-billet interface (affecting the FEM point tracking), and stress tensors extracted from imperfect simulations. Additional model-form uncertainty includes whether isolated pockets of lubricant were present on the billet-billet interface. The billet faces were nominally clean; however, eliminating the presence of all lubricant in metal forming processes is challenging.

5. Discussion

5.1. Accuracy of the new model

Fig. 13 shows the experimental results are dispersed. There is poor reliability regarding the experimental strength obtained at points along or across the welds. Dispersed weld strength results are common in the literature on planar solid-state welding; e.g., in Bay's (1983) and Cooper and Allwood's (2014a) work. However, some trends are clearly visible from Figs. 13 and 15, such as increasing strength towards the rear of the weld, the poor weld strength associated with lubricated surfaces (e.g., when the billet butt is not removed), the increased weld length and strength of two-piece billet welds, and the varying weld strengths along and across the cross-section of non-axisymmetric profiles. The proposed model predicts these experimental trends. However, given the dispersed experimental results, the model should be seen as indicative rather than an accurate predictor of the weld strength. The model results were open-loop predictions for a range of alloys, shapes, and extrusion parameters. Accuracy might be improved with tuning of parameters (e.g., the threshold surface exposure) based on experimental results from similar profiles.

5.2. Industry implications

For traditional extrusion, the new model can be used to help determine whether a weld needs to be removed, to judge the minimum length of profile from the weld nose that must be scrapped, and to help

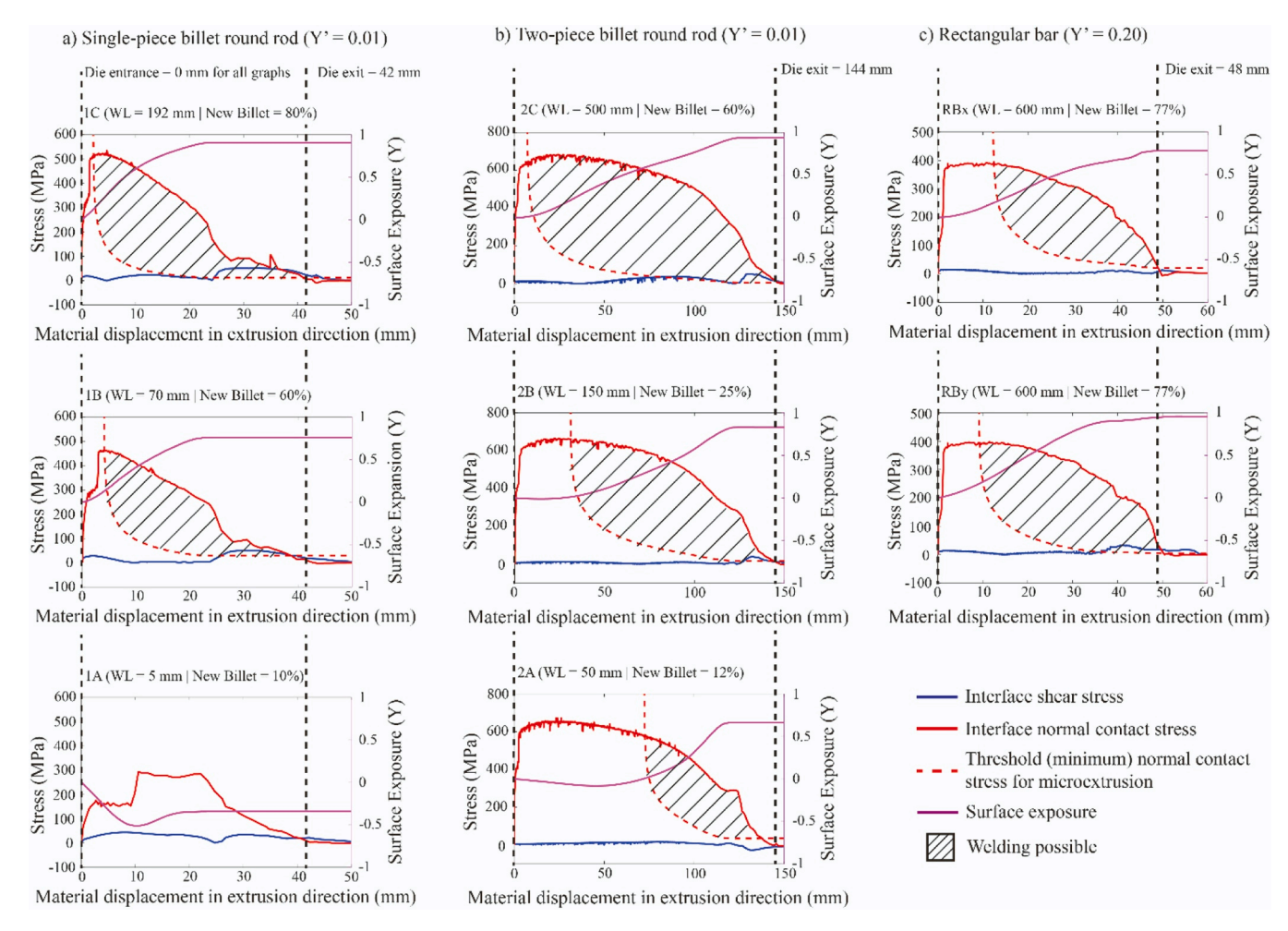


Fig. 14. Surface exposures and stresses along material streamlines from the die entrance to exit. Welding can occur when the normal contact stress exceeds the threshold (minimum). Modeled for $\gamma = 0$.

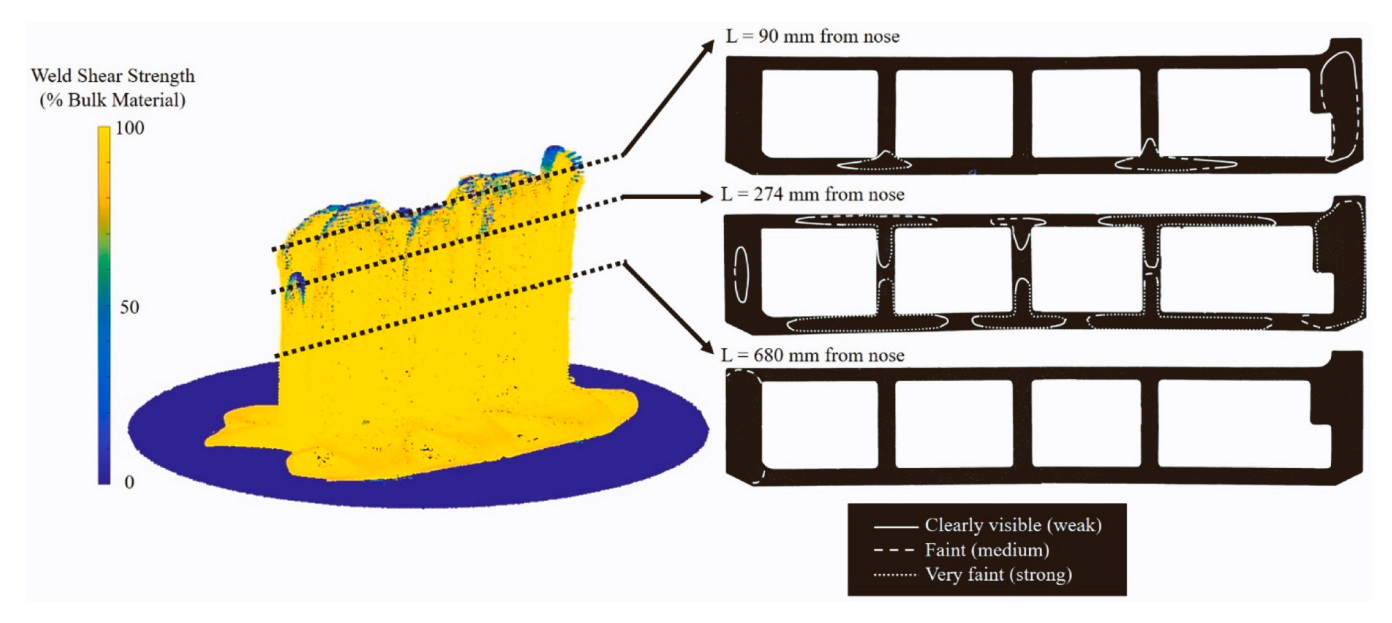


Fig. 15. Predicted (left, $\gamma = 0$) transverse weld strengths versus experimental weld visibility (right) for the complex multi-hollow profile. The visibility of the welding interfaces on the right-hand side has been enhanced for the sake of clarity. The original images (without enhancement but with the ability to zoom) can be downloaded at Oberhausen and Cooper (2023b).

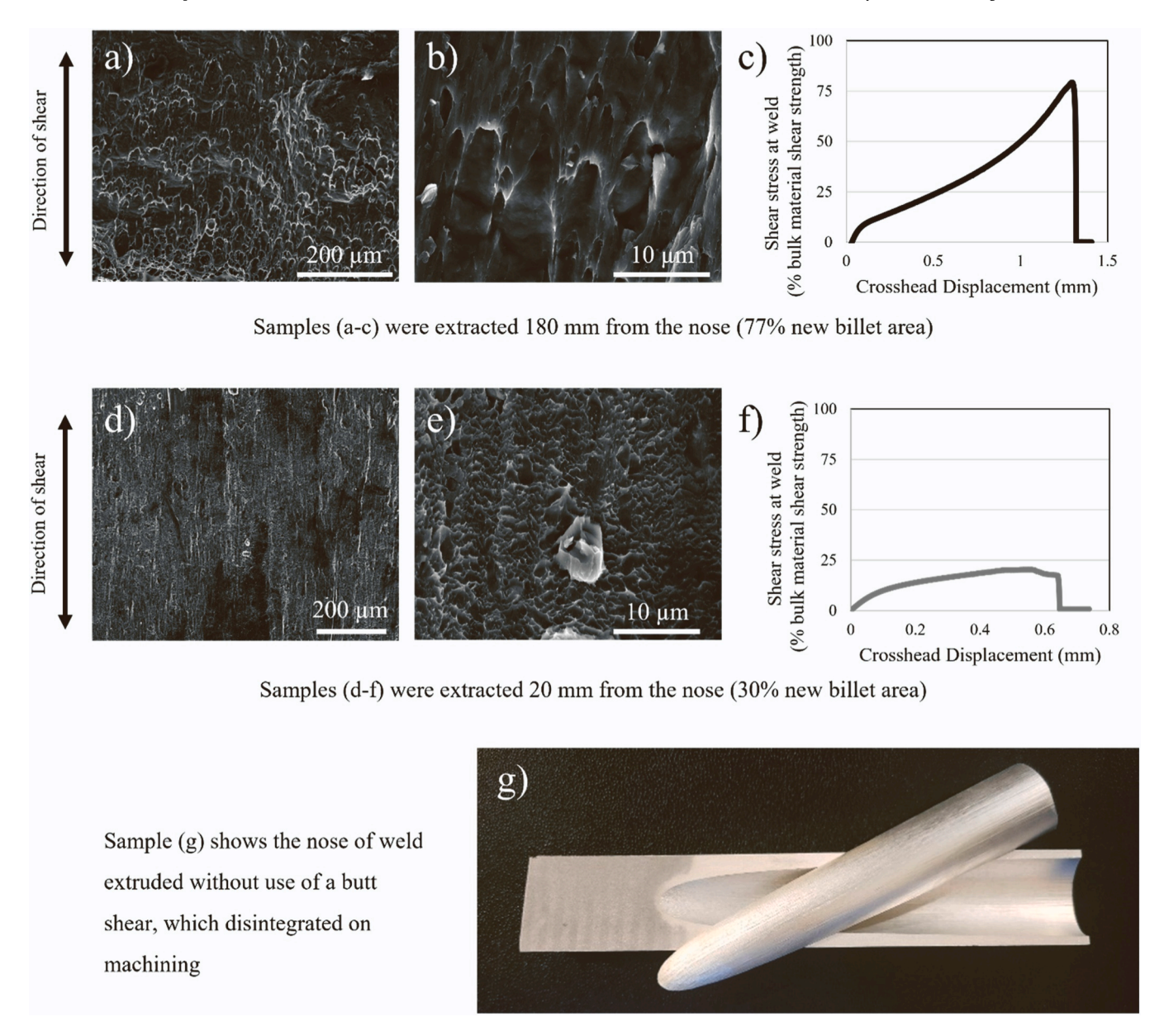


Fig. 16. Shear test fracture morphology. The samples were extracted from the AA6061 round bar, single-piece billet extrusion, with butt shear (except where specified otherwise).

optimize die design for maximum transverse weld strength. The model can also be used to predict weld strengths in novel extrusion processes being studied by researchers. For example, in Lv et al. (2023) multi-container extrusion method for manufacturing wide aluminum profiles where multiple billets with oxide-covered surfaces are welded in the die orifice, or in Oberhausen and Cooper's (2023a) profiled dummy block method for reducing process scrap and starting with a non-planar billet-billet interface.

5.2.1. Surface exposure as the key determinant of transverse weld strength Fig. 14 shows that even for points that form weak welds (e.g., 1A), the normal contact stress is at least three times greater than the yield strength of the hot billet material. Therefore, the pressures in hot extrusion are likely always sufficient to establish close contact between the billet-billet surfaces and exceed the minimum micro-extrusion pressure (shown in Fig. 6b) needed to micro-extrude the substrate through any oxide cracks. The Fig. 5 microscopy also indicates that substrate-to-substrate contact is achieved wherever there are oxide cracks. Subsequently, the fraction of the final contact area that is

exposed aluminum, ν in Eq. 1, is the key determinant of hot extrusion transverse weld strength. ν is largely determined by the surface exposure. The importance of the surface exposure is illustrated in Fig. 17 by plotting the strain history of points that formed strong and weak welds in the experiments. At one extreme there are locations near the nose of the round bar profiles that experience a net negative surface exposure, as observed in Fig. 5c, and possess only handling strength. At the other extreme, several shear test samples display bulk metal strength if extracted from a point that experienced a surface exposure of around 0.95.

Surface exposures vary across as well as along profiles. Fig. 17 highlights that at the same axial distance from the weld nose, a point on the minor axis of the rectangular bar weld experiences a greater surface exposure than a point on the major axis. Both points experience a similar tensile strain but varying perpendicular compressive strains. These compressive strains reduce the surface exposure and correspond to high curvature portions of the weld cross-section. Similarly, Fig. 15 shows regions of greatest weld visibility and lowest strength in areas of high weld line curvatures. This knowledge might be used to inform extrusion

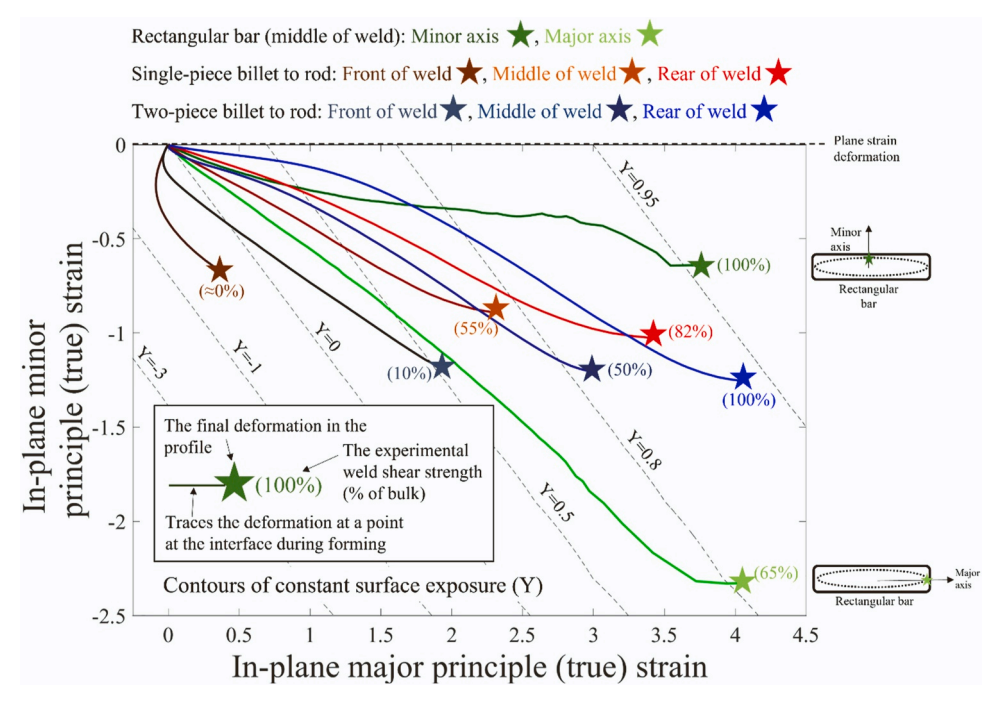


Fig. 17. Plot of principal in-plane strain histories for points along the bonding interface.

profile and die design and, for those cases where the weld is not removed, inform the likelihood of failure if adding fasteners around the outside of the profile.

5.2.2. Reusing process scrap using two-piece billets

For the two-piece billet round rod extrusion, the weld was four times longer than in the single-piece billet case (2000 mm versus 500 mm). Despite this, the two-piece billet weld possesses similar weld strengths to the single-piece billet weld at the same distance from the weld nose (Fig. 13a and b) and exhibits bulk strength long before the weld rear. This is because, for the same percentage area of new billet at the cross-section, the two-piece billet weld experiences greater surface exposures (Fig. 17) and greater oxide spacings (Fig. 4) than the single-piece equivalent. This suggests that the two-piece billet extrusions could be used for more critical components, providing more opportunities for billet scrap reuse, especially if the front section of the elongated weld is removed.

5.2.3. Lubrication and the billet butt shear

The effect of lubrication at the interface is severe. The transverse weld section in profiles produced without use of a butt shear (profiles produced by a minority of extruders using old presses and as explored in some new tooling concepts) is likely unusable even in non-safety critical applications. More generally, every effort should be made to minimize the lubricity of the billet surfaces by minimizing lubricant transfer from billet cutting saws or the butt shear; e.g., using minimum quantity lubrication methods such as supercritical $\rm CO_2$ for cutting ($\rm Cai\ et\ al.,\ 2021$).

6. Conclusions

Concern regarding transverse weld strength is the greatest source of material inefficiency in aluminum extrusion. The main contribution of this work has been to conduct a study on the fragmentation of oxides at the billet-billet interface and to use the findings to update a plane strain film theory model of solid-state welding to non-plane strain conditions, applying it to predict local transverse weld strengths. The oxide fragmentation study showed that local surface contraction results in interface buckling, limited oxide cracking, and weak resulting welds. In

contrast, local surface expansion results in oxide fragments that are equally spaced (locally) in the axial and circumferential directions with dimensions predictable using shear lag modeling and of the order of 36 nm. A significant fraction of the bonding interface (25% in the experiments) displayed incoherent oxide fragmentation where oxides on opposite sides of the interface break-up at different locations, greatly increasing the threshold surface expansions necessary for bonding to initiate. To evaluate the new weld strength model, transverse weld strengths along and across simple and complex profiles were measured experimentally. Unlike in previous work, the weld strengths were determined using sample geometries that isolate the transverse weld and provide a direct measure of weld strength. The experiments show the sensitivity of the weld strength to the starting position of the billet-billet interface (e.g., single-piece vs. two-piece billets). For example, in the axisymmetric case study, the two-piece billet extrusion resulted in a transverse weld 300% longer than the single-piece equivalent. However, the two-piece billet weld reached bulk material strength at a distance from the weld nose equal to just 16% of the weld length. In contrast, no samples extracted from the single-piece billet axisymmetric weld exhibited bulk metal strength. The experiments also show the sensitivity of the weld strength to the position on the weld across as well as along the profile with weld strengths lower in higher curvature portions of the weld. In the experiments, the weld strengths measured along the minor axis of a rectangular profile weld were on average 51% higher than on the major axis.

The new transverse weld strength model predicts the experimental trends and indicates that the weld strength in hot extrusion is not limited by the normal contact stresses at the billet-billet interface. The normal contact stress at the billet-billet interface in the experiments was typically 300–600 MPa, at least four times greater than the hot billet flow stress. Therefore, the die pressures are sufficient to ensure intimate contact and micro-extrusion of substrate through any cracks in the interface oxides. The strength is instead limited by the ability to generate large positive surface expansions across the billet-billet interface, exposing reactive substrate for bonding. Any lubricant at the interface has a deleterious effect. The new model can be used to help determine whether a weld needs to be removed for a given application, to help estimate the minimum length of profile that must be scrapped to ensure the remaining profile contains only strong welds, and to improve die

design and profile design to reduce the impact of transverse welds. These developments can help decarbonize the extrusion industry through increasing manufacturing process yields.

CRediT authorship contribution statement

Gregory Oberhausen: Methodology, Software, Investigation, Formal analysis, Writing – original draft, Writing – review & editing. **Daniel Cooper:** Conceptualization, Methodology, Supervision, Writing – original draft, Writing – review & editing.

Declaration of Competing Interest

The authors declare that they have no known competing financial interests or personal relationships that could have appeared to influence the work reported in this paper.

Data availability

Data will be made available on request.

Acknowledgements

This material is based upon work supported by the National Science Foundation under Grant No. #2122515, the Michigan Translational Research and Commercialization (MTRAC) program, and Ford Motor Company. The authors are also grateful for discussions with industrial partners Hydro and Thumb Tool & Engineering. Any errors are solely the responsibility of the authors.

References

- Afseth, A. (2021). Aluminum Battery Enclosure Design [Webinar]. [Online]. Constellium, Feb. 2021.
- Agrawal, D.C., Raj, R., 1989. Measurement of the ultimate shear strength of a metal-ceramic interface. Acta Metall. 37 (4), 1265–1270. https://doi.org/10.1016/0001-6160(89)00170.
- Akeret, R., 1972. Properties of pressure welds in extruded aluminum alloy sections. J. Inst. Met. 100, 202–207.
- Aluminum Extruders Council. 2022. Body & Chassis Structures Rockers. (https://www.aec.org/page/automotive-rockers). Last Accessed: October 3rd 2022.
- ASTM. 2010. ASTM B831–05 Standard Test Method for Shear Testing of Thin Aluminum Alloy Products.
- Bai, S.W., Fang, G., Zhou, J., 2017. Analysis of the bonding strength and microstructure of AA6082 extrusion weld seams formed during physical simulation. J. Mater. Process. Technol. 250, 109–120. https://doi.org/10.1016/j. jmatprotec.2017.07.012.
- Bai, S.W., Fang, G., Zhou, J., 2019. Integrated physical and numerical simulations of weld seam formation during extrusion of magnesium alloy. J. Mater. Process. Technol. 266 (August 2018), 82–95. https://doi.org/10.1016/j. jmatprotec.2018.10.025.
- Bambach, M., Pietryga, M., Mikloweit, A., Hirt, G., 2014. A finite element framework for the evolution of bond strength in joining-by-forming processes. J. Mater. Process. Technol. 214 (10), 2156–2168.
- Bay, N., 1983. Mechanisms producing metallic bonds in cold welding. Weld. J. 137s $-142s\ https://doi.org/10.1093/jpids/pix105/4823046.$
- Cai, C., Liang, X., An, Q., Tao, Z., Ming, W., Chen, M., 2021. Cooling/Lubrication Performance of Dry and Supercritical CO₂-Based minimum quantity lubrication in peripheral milling Ti-6Al-4V. Int. J. Precis. Eng. Manuf. Green. Technol. 8 (2), 405–421. https://doi.org/10.1007/s40684-020-00194-7.
- Cai, W., Daehn, G., Li, J., Mishra, R., Vivek, A., Khan, H., Komarasamy, M., 2018. A state-of-the-art review on solid-state metal joining. J. Manuf. Sci. Eng. C. https://doi.org/10.1115/1.4041182.
- Chen, L., Zhao, G., Yu, J., Zhang, W., 2015. Evaluation of a pyramid die extrusion for a hollow aluminum profile using FE simulation. J. Mech. Sci. Technol. 29 (5), 2195–2203. https://doi.org/10.1007/s12206-015-0440-3.
- Cooper, D.R., Allwood, J.M., 2014a. The influence of deformation conditions in solidstate aluminium welding processes on the resulting weld strength. Journal of Materials Processing Technology 214 (2014), 2576–2592.
- Cooper, D.R., Allwood, J.M., 2014b. Influence of diffusion mechanisms in aluminium solid-state welding processes. Procedia Eng. 81 (October), 2147–2152. doi:10.1016/ j.proeng.2014.10.300.
- Crosio, M., Hora, D., Becker, C., Hora, P., 2018. Realistic representation and investigation of charge weld evolution during direct porthole die extrusion processes through FE-analysis. Procedia Manuf. 15, 232–239. https://doi.org/10.1016/j. promfg.2018.07.214.

- da Silva, T. (2016). The Extrusion of Two-Piece Billets. International Aluminum Extrusion Technology Seminar, 239–254.
- den Bakker, A.J., Katgerman, L., van der Zwaag, S., 2016. Analysis of the structure and resulting mechanical properties of aluminium extrusions containing a charge weld interface. J. Mater. Process. Technol. 229, 9–21. https://doi.org/10.1016/j. imatprotec.2015.09.013.
- Ding, S., Shi, Q., Chen, G., 2021. Flow stress of 6061 aluminum alloy at typical temperatures during friction stir welding based on hot compression tests. Metals 11 (5). https://doi.org/10.3390/met11050804.
- Donati, L., Tomesani, L., 2004. Evaluation Of a new FEM criterion for seam welds quality prediction in aluminum extruded profiles. Proc. Eighth Int. Alum. Extrus. Technol. Semin. 221–235.
- Donati, L., Tomesani, L., 2008. Seam welds modeling and mechanical properties prediction in the extrusion of AA6082 alloy. Key Eng. Mater. 367, 125–136. https://doi.org/10.4028/0-87849-467-7.125.
- Edwards, S.P., den Bakker, A.J., Zhou, J., Katgerman, L., 2009. Physical simulation of longitudinal weld seam formation during extrusion to produce hollow aluminum profiles. Mater. Manuf. Process. 24 (4), 409–421. https://doi.org/10.1080/ 10426910802714290.
- Edwards, S.P., den Bakker, A.J., Neijenhuis, J.L., Kool, W.H., Katgerman, L., 2006. The influence of the solid-state bonding process on the mechanical integrity of longitudinal weld seams. JSME Int. J. Ser. A: Solid Mech. Mater. Eng. 49 (1), 63–68. https://doi.org/10.1299/jsmea.49.63.
- Evertsson, J., Bertram, F., Zhang, F., Rullik, L., Merte, L.R., Shipilin, M., Soldemo, M., Ahmadi, S., Vinogradov, N., Carlà, F., Weissenrieder, J., Göthelid, M., Pan, J., Mikkelsen, A., Nilsson, J.O., Lundgren, E., 2015. The thickness of native oxides on aluminum alloys and single crystals. Appl. Surf. Sci. 349, 826–832. https://doi.org/10.1016/j.apsusc.2015.05.043.
- Ford Motor Company. 2014. Mechanical Properties Measurements after Thermal Processing of Aluminum Alloy, FORD WSS-M2A177, December 17, 2014. (https://standards.globalspec.com/std/1693197/FORD%20WSS-M2A177-A1).
- Ghalehbandi, S.M., Malaki, M., Gupta, M., 2019. Accumulative roll bonding a review. Appl. Sci. 9, 3627.
- Grigoriev, A.Y., 2015. Slope angles of rough surface asperities after machining. J. Frict. Wear 36 (3), 197–199. https://doi.org/10.3103/S106836661503006X.
- Hatzenbichler, T., Buchmayr, B., 2010. Finite element method simulation of internal defects in billet-to-billet extrusion. Proc. Inst. Mech. Eng., Part B: J. Eng. Manuf. 224 (7), 1029–1042. https://doi.org/10.1243/09544054JEM1830.
- Heinemann, H.H. (1961). Flow Stress of Different Aluminum and Copper Alloys for High Strain Rates and Temperature. PhD Thesis.
- IEA. 2019. Material efficiency in clean energy transitions. Report: International Energy Agency, Paris. (https://www.iea.org/reports/material-efficiency-in-clean-energy-transitions).
- Kniazkin, I., Vlasov, A., 2020. Quality prediction of longitudinal seam welds in aluminium profile extrusion based on simulation. Procedia Manuf. 50 (2019), 433–438. https://doi.org/10.1016/j.promfg.2020.08.079.
- Kolpak, F., Schulze, A., Dahnke, C., Tekkaya, A.E., 2019. Predicting weld-quality in direct hot extrusion of aluminium chips. J. Mater. Process. Tech. 274 (April), 116294 https://doi.org/10.1016/j.jmatprotec.2019.116294.
- Le, H.R., Sutcliffe, M.P.F., Wang, P.Z., Burstein, G.T., 2004. Surface oxide fracture in cold aluminium rolling. Acta Materialia 52 (2004), 911–920.
- Lennon, A., Lunardi, M., Hallam, B., Dias, P.R., 2022. The aluminium demand risk of terawatt photovoltaics for net zero emissions by 2050. Nat. Sustain. 5 (4), 357–363. https://doi.org/10.1038/s41893-021-00838-9.
- Liu, Z., Li, L., Yi, J., Li, S., Wang, G., 2017. Influence of extrusion speed on the seam weld quality in the porthole die extrusion of AZ31 magnesium alloy tube. Int. J. Adv. Manuf. Technol. 92 (1–4), 1039–1052. https://doi.org/10.1007/s00170-017-0200-
- Lou, S., Wang, A., Lu, S., Guo, G., Qu, C., Su, C., 2019. Tensile property and micro-texture evolution of the charge weld in a billet-to-billet extrusion of AA6061 aluminum profile. Int. J. Adv. Manuf. Technol. 103 (1–4), 1309–1323. https://doi.org/ 10.1007/s00170-019-03573-w.
- Lv, J., Yu, J., Shi, Z., Li, W., Lin, J., 2023. Feasibility study of a novel multi-container extrusion method for manufacturing wide aluminium profiles with low force. J. Manuf. Process. 85, 584–593.
- Mag Specialties. (2019). A series of roundtable discussions between a Research & Development Engineer at Mag Specialties and the current article's authors (June-August 2019).
- Mahmoodkhani, Y., Wells, M.A., Parson, N., Poole, W.J., 2014. Numerical modelling of the material flow during extrusion of aluminium alloys and transverse weld formation. J. Mater. Process. Technol. 214 (3), 688–700. https://doi.org/10.1016/j. imatprotec.2013.09.028.
- Merklein, M., Biasutti, M., 2011. Forward and reverse simple shear test experiments for material modeling in forming simulations. In: Hirt, G., Tekkaya, A.E. (Eds.), International Conference on Technology of Plasticity, pp. 702–707.
- Nanninga, N., White, C., Dickson, R., 2011. Charge weld effects on high cycle fatigue behavior of a hollow extruded AA6082 profile. J. Mater. Eng. Perform. 20 (7), 1235–1241. https://doi.org/10.1007/s11665-010-9755-5.
- Nicholas, M., 1990. In: North, T. (Ed.), Material Aspects of Ceramic–Ceramic and Ceramic–Metal Bonding. Springer, New York, pp. 160–173. ISBN-10: 0412386003.
- Oberhausen, G.J., Zhu, Y., Cooper, D.R., 2022. Reducing the environmental impacts of aluminum extrusion. Resour., Conserv. Recycl. 179, 106120 https://doi.org/10.1016/j.resconrec.2021.106120.
- Oberhausen, G.J., Christopher, A.A.A., Cooper, D.R. 2021. Reducing aluminum extrusion transverse weld process scrap. Proceedings of the International Conference on the Technologies of Plasticity.

- Oberhausen, G.J., Cooper, D.R. 2023b. Images of complex hollow profile cross-section showing the transverse weld interface across the profile. URL = $\langle https://remade.engin.umich.edu/images/hollow_weld_strength.jpg \rangle$.
- Oberhausen, G.J., Cooper, D.R. 2023a. Exploring a novel process for reducing aluminum extrusion process scrap. Proceedings of the International Conference on the Technologies of Plasticity.
- Plata, M., Piwnik, J. 2000. Theoretical and experimental analysis of seam weld formation in hot extrusion of aluminium alloys. 7th International Conference on Aluminum Extrusion Technology.
- Reggiani, B., Segatori, A., Donati, L., Tomesani, L., 2013. Prediction of charge welds in hollow profiles extrusion by FEM simulations and experimental validation. Int. J. Adv. Manuf. Technol. 69, 1855–1872. https://doi.org/10.1007/s00170-013-5143-2.
- Saha, P., 2000. ASM. Aluminum Extrusion Technology. ASM Technical Books,
- Saito, Y., Utsunomiya, H., Tsuji, N., Sakai, T., 1999. Novel ultra-high straining process for bulk materials-development of the accumulative roll-bonding (ARB) process. Acta Mater. 47 (2), 579–583.
- Tang, J., Chen, L., Li, Z., Zhao, G., Zhang, C., Zuo, Y., 2022. Evolution mechanisms of charge weld during porthole die extrusion of ZK60 Mg profile. J. Mater. Process. Technol. 300 https://doi.org/10.1016/j.jmatprotec.2021.117401.
- Tylecote, R.F., 1968. The Solid Phase Welding of Metals. Edward Arnold,
- Wang, Y., Zhao, G., Zhang, W., Sun, L., Wang, X., Lv, Z., 2022. Interfacial bonding mechanism and length evaluation method of the longitudinal welds in the unsteady deformation process of porthole die extrusion of aluminum alloy profiles. J. Mater. Res. Technol. 20, 1624–1644. https://doi.org/10.1016/j.jmrt.2022.07.163.
- Wu, H.-Y., Lee, S., Wang, J.-Y., 1998. Solid-state bonding of iron-based alloys, steel-brass, and aluminum alloys. J. Mater. Process. Technol. Vol. 75.

- Xie, J.X., Murakami, T., Ikeda, K., Takahashi, H.H., 1995. Experimental simulation of metal flow in porthole-die extrusion. J. Mater. Process. Technol. 49 (1-2), 1-11
- Yin, Q., Zillmann, B., Suttner, S., Gerstein, G., Biasutti, M., Tekkaya, A.E., Wagner, M.F. X., Merklein, M., Schaper, M., Halle, T., Brosius, A., 2014. An experimental and numerical investigation of different shear test configurations for sheet metal characterization. Int. J. Solids Struct. 51 (5), 1066–1074. https://doi.org/10.1016/j.iisolstr.2013.12.006.
- Yu, J., Zhao, G., Chen, L., 2016a. Investigation of interface evolution, microstructure and mechanical properties of solid-state bonding seams in hot extrusion process of aluminum alloy profiles. J. Mater. Process. Technol. 230, 153–166.
- Yu, J., Zhao, G., Chen, L., 2016b. Analysis of longitudinal weld seam defects and investigation of solid-state bonding criteria in porthole die extrusion process of aluminum alloy profiles. J. Mater. Process. Technol. 237, 31–47.
- Yu, J., Zhao, G., Zhao, X., Chen, L., Chen, M., 2019. Microstructures of longitudinal/ transverse welds and back-end defects and their influences on the corrosion resistance and mechanical properties of aluminum alloy extrusion profiles. J. Mater. Process. Technol. 267, 1–16. https://doi.org/10.1016/j.jmatprotec.2018.12.006.
- Zhang, C., Dong, Y., Wang, C., Zhao, G., Chen, L., Sun, W., 2017. Evolution of transverse weld during porthole extrusion of AA7N01 hollow profile. J. Mater. Process. Technol. 248 (January), 103–114. https://doi.org/10.1016/j.jmatprotec.2017.05.017.
- Zhang, X.M., Feng, D., Shi, X.K., Liu, S.D., 2013. Oxide distribution and microstructure in welding zones from porthole die extrusion. Trans. Nonferrous Met. Soc. China 23 (3), 765–772. https://doi.org/10.1016/S1003-6326(13)62527-3.